Geochemistry Geophysics Geosystems G3
AN ELECTRONIC JOURNAL OF THE EARTH SCIENCES
Published by AGU and the Geochemical Society

Article
Volume 7, Number 6
8 June 2006
Q06006, doi:10.1029/2005GC001141
ISSN: 1525-2027

Paleointensity applications to timing and extent of eruptive activity, 9°–10°N East Pacific Rise

Julie Bowles and Jeffrey S. Gee
Scripps Institution of Oceanography, University of California, San Diego, 9500 Gilman Drive, MC 0220, La Jolla, California 92093, USA (jbowles@ucsd.edu)

Dennis V. Kent
Department of Geological Sciences, Rutgers University, 610 Taylor Road, Piscataway, New Jersey 08854–8066, USA

Also at Lamont-Doherty Earth Observatory of Columbia University, 61 Route 9W, Palisades, New York 10964–8000, USA

Michael R. Perfit
Department of Geological Sciences, University of Florida, 241 Williamson Hall, Gainesville, Florida 32611–2120, USA

S. Adam Soule and Daniel J. Fornari
Woods Hole Oceanographic Institution, Woods Hole, Massachusett 02543–1050, USA

[1] Placing accurate age constraints on near-axis lava flows has become increasingly important given the structural and volcanic complexity of the neovolcanic zone at fast spreading ridges. Geomagnetic paleointensity of submarine basaltic glass (SBG) holds promise for placing quantitative age constraints on near-axis flows. In one of the first extensive tests of paleointensity as a dating tool or temporal marker we present the results of over 550 successful SBG paleointensity estimates from 189 near-axis (<4 km) sites at the East Pacific Rise, 9°–10°N. Paleointensities range from 6 to 53 μT and spatially correspond to the pattern expected from known temporal variations in the geomagnetic field. Samples within and adjacent to the axial summit trough (AST) have values approximately equal to or slightly higher than the present-day. Samples out to 1–3 km from the AST have values higher than the present-day, and samples farther off axis have values lower than the present-day. The on-axis samples (<500 m from the AST) provide a test case for using models of paleofield variation for the past few hundred years as an absolute dating technique. Results from samples collected near a well-documented eruption in 1991–1992 suggest there may be a small negative bias in the paleointensity estimates, limiting resolution of the dating technique. Possible explanations for such a bias include local field anomalies produced by preexisting magnetic terrain; anomalously high magnetic unblocking temperatures, leading to a small cooling rate bias; and/or the possibility of a chemical remanence produced by in situ alteration of samples likely to have complicated thermal histories. Paleointensity remains useful in approximating age differences in young flows, and a clear along-axis paleointensity contrast near 9°50′N is suggestive of a ~150–200 year age difference. Paleointensity values of off-axis samples are generally consistent with rough age interpretations based on side scan data. Furthermore, spatial patterns in the paleointensity suggest extensive off-axis flow emplacement may occur infrequently, with recurrence intervals of 10–20 kyr. Results of a stochastic model of lava emplacement show that this can be achieved with a single distribution of flows, with flow size linked to time between eruptions.

Components: 20,312 words, 14 figures, 2 tables, 1 dataset.

Index Terms: 1521 Geomagnetism and Paleomagnetism: Paleointensity; 1527 Geomagnetism and Paleomagnetism: Paleomagnetism applied to geologic processes; 3035 Marine Geology and Geophysics: Midocean ridge processes.

Received 13 September 2005; **Revised** 23 November 2005; **Accepted** 2 February 2006; **Published** 8 June 2006.

Bowles, J., J. S. Gee, D. V. Kent, M. R. Perfit, S. A. Soule, and D. J. Fornari (2006), Paleointensity applications to timing and extent of eruptive activity, 9°–10°N East Pacific Rise, *Geochem. Geophys. Geosyst.*, *7*, Q06006, doi:10.1029/2005GC001141.

1. Introduction

[2] Our understanding of the neovolcanic zone at fast spreading ridges, especially the East Pacific Rise (EPR), has evolved and become increasingly sophisticated in recent years as higher-resolution observations become available. From a basic understanding of a narrow (<250–2000 m) region centered on the axial summit and covered by small-volume flows [*Macdonald et al.*, 1984, 1992; *Haymon et al.*, 1991; *Perfit and Chadwick*, 1998; *Fornari et al.*, 1998], the neovolcanic zone at fast spreading ridges is now estimated to be up to 4 km wide, with volcanic contributions both from flows erupted at or near the axial summit and channeled off-axis in a dendritic network of lava channels, and from some off-axis constructional volcanism [e.g., *Fornari et al.*, 1998, 2004; *Soule et al.*, 2005]. Relatively small-volume ($\sim 10^6$ m^3) eruptions predominate, emanating from fissures ~1 to >18 km in length along axis [*Gregg et al.*, 1996; *Sinton et al.*, 2002], with occasional contributions from larger volume flows [*Fornari et al.*, 1998, 2004; *Kurras et al.*, 2000].

[3] Eruptive recurrence intervals at fast spreading ridges are hypothesized to be on the order of years to tens of years [*Perfit and Chadwick*, 1998; *Sinton et al.*, 2002], and observational evidence combined with limited radiometric dating suggests that at least in places much of the surface out to two kilometers from the axis is less than 2 kyr old [*Fornari et al.*, 2004; *Sims et al.*, 2003]. Putting more precise constraints on absolute and/or relative ages between flows or flow groups is difficult. The degree of sediment cover or Mn coating, especially in areas distant from hydrothermal vents, can provide a rough idea of age or relative age, but sediment accumulation rates and degree of Mn coating can vary greatly, both in space and time [e.g., *Haymon et al.*, 1991]. Other observational evidence, such as degree of faulting or the biological assemblages present, can also sometimes provide gross relative age estimates. When flow boundaries can be directly observed, normal rules of superposition can provide relative ages, but it is generally not possible to determine if two flows were separated in time by weeks, years or centuries. Extensive mapping of some areas by high-resolution side scan has provided information on relative ages on a much larger scale than a single *Alvin* dive [e.g., *Fornari et al.*, 2004; *Soule et al.*, 2005]. Areas mostly covered by young versus old flows can be distinguished on the basis of the intensity and character of the backscatter, which is primarily related to the volcanic morphology, but is also influenced by seafloor slope and sediment cover.

[4] Radiometric dating has proved valuable in recognizing that while some EPR flows have ages nearly equal to their spreading rate age, some flows have erupted or flowed off axis and are significantly younger than would be expected on the basis of their distance from the axis [e.g., *Goldstein et al.*, 1994; *Sims et al.*, 2003]. However, most isotope systematics are poorly suited to distinguishing ages on timescales of 10s to 100s of years. While ^{210}Po-^{210}Pb can provide very accurate dates for flows less than a few years old [e.g., *Rubin et al.*, 1994], and a relatively new technique using ^{210}Pb-^{226}Ra provides some ability to establish whether a flow is less than or greater than ~100 years old [*Rubin et al.*, 2005; *Bergmanis et al.*, 2004], other U series disequilibria [e.g., *Rubin and Macdougall*, 1990; *Goldstein et al.*, 1994; *Sims et al.*, 2003] are limited by incomplete knowledge of the timing and degree of the initial disequilibrium. Though the half-life of ^{226}Ra-^{230}Th disequilibrium is well suited to providing age information for samples <8 ka, and ^{238}U-^{230}Th for samples <375 ka [*Macdougall*, 1995], resolution is likely on the order of thousands of years. Though U series disequilibria have proved valuable in examining magma genesis, transport and storage processes, they are inherently limited in their ability to accurately determine actual eruption ages. For most on-axis flows the relatively subjective observational evidence remains the only way to approximate age.

[5] Geochemical mapping may distinguish one flow field or event as temporally or spatially distinct from another. While this has been suggested as a means of distinguishing lavas erupted

off- versus on-axis [*Reynolds and Langmuir*, 2000; *Perfit et al.*, 1994], some evidence suggests its usefulness in delineating individual events may be limited. For example, the Aldo Kihi flow field at 17°24–17°34′S on the EPR is thought to have erupted over a very limited time interval, yet shows rather heterogeneous geochemistry [*Sinton et al.*, 2002]. In some cases the flow can be clearly distinguished compositionally from older lavas, but in others there is no geochemical difference across flow boundaries. At ~9°50′N, an eruption in late 1991 or early 1992 produced lavas ~5 km north of the main flow with a distinct composition, despite being demonstrably part of the same event [*Haymon et al.*, 1993; *Perfit et al.*, 1994; *Rubin et al.*, 2001].

[6] The ability to provide reliable absolute or relative age constraints on flows <500 years old using traditional methods outlined above remains elusive. However, recent studies [*Carlut and Kent*, 2000; *Gee et al.*, 2000] suggest that geomagnetic paleointensity estimates from submarine basaltic glass (SBG) might be used, in conjunction with geomagnetic field models [e.g., *Jackson et al.*, 2000], to determine eruptive ages for very young (<150 year) mid-ocean ridge lavas. By making some reasonable assumptions about field behavior for the past 40–60 kyr, we can further place relative age constraints on samples older than 150 years. *Bowles et al.* [2005] show that a series of samples from 17°–18°S on the EPR yield paleointensity ages (from 0 to ~1–2 ka) consistent with all available observational and radiometric information. *Carlut et al.* [2004] have used paleointensity variations over longer timescales (0–40 kyr) to place broad relative age constraints on sections of the EPR from 15°22′N–18°N. *Mejia et al.* [1996] show SBG paleointensity results from ~9°30′N on the EPR that are consistent with known variations in the geomagnetic field.

[7] SBG is often considered to be an excellent recorder of field intensity. It demonstrates ideal behavior in stepwise reheating experiments designed to recover paleointensity estimates, primarily because of the small grain size of the magnetic particles. The composition of the particles appears to be Ti-poor titanomagnetite [*Pick and Tauxe*, 1994], an observation that has caused some concern [e.g., *Heller et al.*, 2002; *Smirnov and Tarduno*, 2003; *Morales et al.*, 2003; *Goguitchaichvili et al.*, 2004] because low-Ti magnetite is not an equilibrium phase in basaltic melt. Glass is not an equilibrium phase, however, and departures from equilibrium are not unexpected [*Zhou et al.*, 2000]. Nevertheless, this low-Ti composition has led to speculations that the magnetic remanence in SBG is a secondary (low-temperature) chemical remanence, rather than a primary thermal remanence [*Heller et al.*, 2002], which could lead to invalid paleointensity estimates from SBG. While acknowledging that the exact mechanism of magnetite formation in glass remains poorly understood, a growing body of work provides evidence that the remanence is thermal and that SBG accurately records the field. Among the evidence summarized by *Tauxe and Staudigel* [2004] and *Bowles et al.* [2005] is the observation that magnetization strength and grain size appear to increase with distance inward from the chilled margin [*Zhou et al.*, 2000; *Carlut and Kent*, 2002; *Bowles et al.*, 2005]; this argues against postemplacement alteration as the source of the remanence, which should proceed from the outside inward. Agreement between SBG paleointensity and known field values [*Pick and Tauxe*, 1993; *Mejia et al.*, 1996; *Carlut and Kent*, 2000; *Bowles et al.*, 2005] also strongly suggests a primary thermoremanence.

[8] The 9°–10°N segment of the East Pacific Rise is an ideal location to further test the validity of SBG paleointensity and paleointensity dating methods. Intensive mapping and characterization efforts along the length of the segment provide abundant observational and geochemical data against which to compare the paleomagnetic age estimates [e.g., *Macdonald et al.*, 1992; *Haymon et al.*, 1991, 1993; *Perfit et al.*, 1994; *Fornari et al.*, 1998; *Kurras et al.*, 2000; *Smith et al.*, 2001; *White et al.*, 2002; *Fornari et al.*, 2004; *Soule et al.*, 2005]. Using submarine basaltic glass (SBG) collected from ±4 km of the EPR crest between 9°17′ and 9°55′N, we further assess the feasibility of using paleointensity to provide dating at decade to century-scale resolution, timescales over which radiometric dating is the least effective. We also examine paleointensity and near-ridge volcanism in the context of longer-term changes in field intensity. The data allow us to examine variations in eruptive activity both along and across axis, addressing recurrence intervals on axis, the aerial extent of the neovolcanic zone, and the episodicity of extensive off-axis volcanism.

2. Geologic Setting and Sampling

[9] Located between the Siqueiros and Clipperton fracture zones (Figure 1a), the 9°–10°N segment of

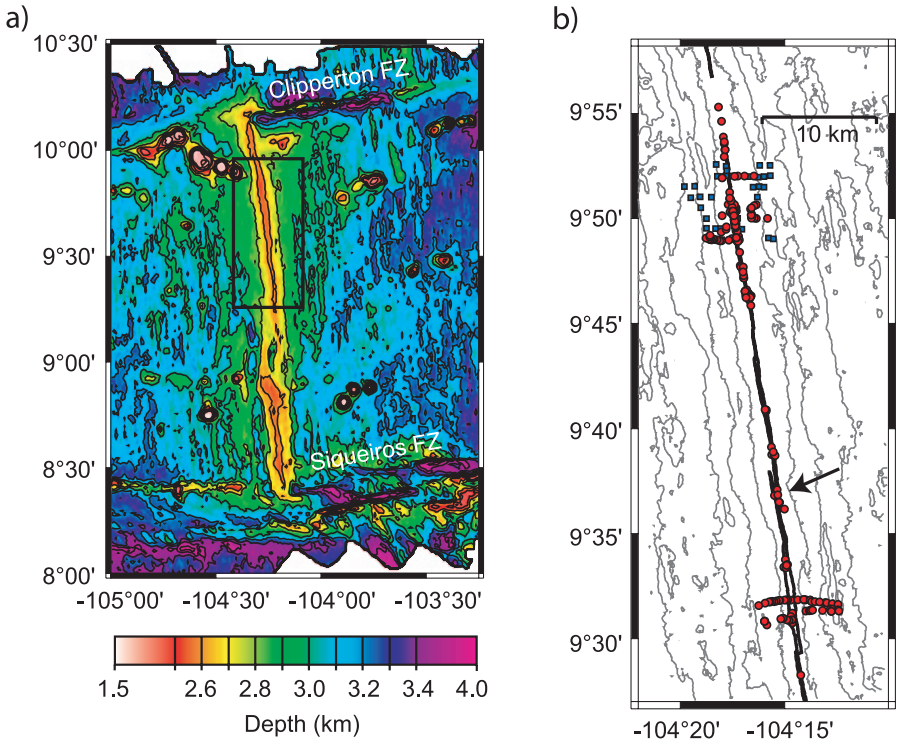

Figure 1. Study and sample location maps. (a) Overview bathymetry map of the 9°N segment of the East Pacific Rise [*Macdonald et al.*, 1992]. Study area (box) is situated north of the OSC at 9°N. The 200 m contours are shown in black. (b) Close-up of study area shown by box in Figure 1a. Samples selected for analysis were collected by DSV *Alvin* (red circles) or via rock core (blue squares). Bounds of axial summit trough [from *Fornari et al.*, 2004, also manuscript in preparation] are shown by heavy black line. Arrow indicates location of small OSC at 9°37′N. Not shown are two samples taken from axis at ~9°17′N. The 100 m contours [*Cochran et al.*, 1999] are shown in light gray lines.

the EPR has spread symmetrically for at least the last few million years at a half-rate of 54 mm yr^{-1}, based on an age of 0.78 Ma for the Brunhes-Matuyama reversal boundary [*Carbotte and Macdonald*, 1992; *Cande and Kent*, 1995]. The study area encompasses the northern part of the segment (~9°17′–9°55′N), north of a large overlapping spreading center (OSC) at 9°03′N. This second-order segment is characterized by a broad, shallow, axial high [*Macdonald and Fox*, 1988], with an axial summit collapse trough (AST) between 9°22′ and 9°52′N formed primarily by lava drain back and collapse [*Haymon et al.*, 1991; *Fornari et al.*, 1998, 2004]. The second-order segment is further subdivided by a smaller OSC, or axial discontinuity, at 9°37′N into a more magmatically robust section to the north and a comparatively magma-starved section to the south [*Smith et al.*, 2001].

[10] Samples selected for analysis (Figure 1b) are concentrated in two regions, centered roughly at 9°31′N and 9°50′N, to the south and north of the smaller OSC, respectively. Most samples were collected via *Alvin* submersible and are located to better than 50 m, with more recent dives located to better than 20 m. A few samples (squares in Figure 1b) were collected with wax cores from the surface ship, and are located only to within ~200–400 m. Samples from *Alvin* dives 3784 and 3963 were provided by M. Tivey. Sample coordinates are given in Table 1.

[11] The region around 9°50′N is the shallowest portion of the segment, and is characterized either by a narrow (40–80 m) and shallow (<10 m) AST, indicative of frequent volcanic activity, or by sets of narrow, en echelon fissures in areas where presumably the AST has been paved over by a recent eruption [*Fornari et al.*, 1998]. Structures interpreted as lava flow channels are abundant, especially at 9°50′N and 9°48N, and appear to be sourced at or near the AST [*Fornari et al.*, 2004; *Soule et al.*, 2005]. In 1991–1992, a fissure eruption occurred between 9°46′ and 9°51′N, filling the trough and in places overflowing or breaching the AST walls [*Haymon et al.*, 1993; *Gregg et al.*, 1996]. (A breaching or "breakout channel" at ~9°50.3′–50.4′N can be seen in sonar and high-

Table 1. Site Locations and Paleointensity Results[a]

Site	Lat, °N	Min Lat	Lon, °W	Min Lon	Dist	N	F_{m1}	σ_1	F_{m2}	σ_2	1991–1992
2739-5	9.2786	16.72	104.2258	13.55	−0.650	6	36.7	0.8	36.7	0.9	
2739-3	9.2793	16.76	104.2190	13.14	0.000	2	34.8	2.9	34.8	2.5	
2365-4	9.2797	16.78	104.2182	13.09	0.200	2	34.6	3.3	36.6	5.0	
2365-3	9.2799	16.79	104.2181	13.09	0.206	7	35.3	0.2	35.7	0.5	
2365-2	9.2801	16.81	104.2188	13.13	0.000	4	31.8	0.9	31.9	1.0	
2374-12	9.4708	28.25	104.2371	14.23	−0.011	4	34.6	2.5	34.6	2.2	
2503-11	9.5108	30.65	104.2641	15.85	−2.334	2	40.6	0.0	40.9	0.5	
2358-11	9.5125	30.75	104.2438	14.63	−0.065	6	40.8	0.9	40.8	1.0	
2358-9	9.5125	30.75	104.2440	14.64	−0.065	7	41.3	1.4	42.1	1.8	
2503-13	9.5135	30.81	104.2661	15.97	−2.556	3	24.7	0.2	24.7	0.5	
2503-14	9.5135	30.81	104.2661	15.97	−2.556	1	19.0	NA	20.0	(1.0)	
2503-12	9.5140	30.84	104.2660	15.96	−2.546	5	36.3	1.1	36.3	1.1	
2503-2	9.5144	30.86	104.2465	14.79	−0.275	6	40.2	1.2	40.9	1.3	
2503-3	9.5144	30.86	104.2465	14.79	−0.280	12	37.8	0.7	37.6	1.1	
2353-5	9.5145	30.87	104.2433	14.60	0.077	4	44.8	1.5	45.6	1.6	
2358-3	9.5146	30.88	104.2442	14.65	−0.022	2	37.9	2.3	38.6	2.5	
2503-1	9.5148	30.89	104.2441	14.65	−0.011	9	38.2	0.9	40.3	1.3	
2503-4	9.5148	30.89	104.2482	14.89	−0.460	3	43.2	3.9	44.3	4.3	
2503-10	9.5157	30.94	104.2530	15.18	−0.998	4	44.2	1.9	44.8	1.8	
2503-6	9.5160	30.96	104.2512	15.07	−0.796	3	44.6	2.9	44.5	2.6	
2503-7	9.5161	30.97	104.2513	15.08	−0.806	4	39.5	2.9	39.9	2.9	
2364-9A	9.5176	31.06	104.2451	14.71	−0.011	3	38.7	1.2	38.2	1.6	
2364-5	9.5200	31.20	104.2444	14.66	0.067	6	40.2	3.3	40.9	2.9	
2364-6	9.5201	31.21	104.2439	14.63	0.122	4	39.0	4.5	39.3	4.0	
2495-8A	9.5215	31.29	104.2126	12.76	3.703	3	20.5	0.1	20.3	0.3	
2495-8C	9.5215	31.29	104.2126	12.76	3.703	3	7.0	0.4	6.9	0.4	
2495-3	9.5220	31.32	104.2303	13.82	1.740	1	6.6	NA	6.5	(0.2)	
2495-7	9.5223	31.34	104.2197	13.18	2.915	2	7.9	0.1	7.8	0.2	
2495-5	9.5224	31.34	104.2291	13.75	1.873	1	11.9	NA	11.8	(0.4)	
2495-6	9.5226	31.36	104.2276	13.66	2.040	4	29.0	0.7	29.1	0.7	
2495-11	9.5227	31.36	104.2073	12.44	4.290	2	9.7	0.1	9.9	0.6	
2495-10	9.5232	31.39	104.2118	12.71	3.791	2	7.4	0.1	7.3	0.3	
2495-9	9.5235	31.41	104.2134	12.80	3.614	2	7.8	0.1	7.9	0.1	
2490-14	9.5261	31.57	104.2708	16.25	−2.860	2	17.5	0.9	17.5	1.0	
2489-12	9.5271	31.63	104.2073	12.44	4.290	2	6.6	0.1	6.6	0.1	
2489-8	9.5276	31.66	104.2119	12.71	3.780	1	7.7	NA	7.7	(0.2)	
2489-6	9.5282	31.69	104.2162	12.97	3.303	2	6.5	0.1	6.5	0.1	
2489-5	9.5285	31.71	104.2175	13.05	3.160	4	14.9	0.6	14.7	0.6	
2490-10	9.5289	31.73	104.2625	15.75	−1.829	2	29.9	5.4	30.8	5.8	
2489-4A	9.5290	31.74	104.2220	13.32	2.661	5	12.5	0.3	12.4	0.2	
2489-3	9.5292	31.75	104.2258	13.55	2.239	2	13.9	0.5	13.8	0.6	
2489-1	9.5293	31.76	104.2283	13.70	1.962	3	15.2	0.8	15.0	0.7	
2490-7	9.5293	31.76	104.2583	15.50	−1.364	2	42.2	1.5	42.7	5.6	
2490-8	9.5294	31.76	104.2601	15.61	−1.563	4	45.0	1.3	44.7	1.8	
2490-6	9.5297	31.78	104.2567	15.40	−1.186	4	46.6	1.5	46.4	1.8	
2490-5	9.5302	31.81	104.2545	15.27	−0.942	3	43.8	1.5	44.3	1.4	
2488-2	9.5304	31.82	104.2452	14.71	0.089	1	49.8	NA	47.9	(2.5)	
2488-7	9.5305	31.83	104.2296	13.78	1.818	1	29.3	NA	29.7	(0.3)	
2488-7A	9.5305	31.83	104.2296	13.78	1.818	5	28.2	1.4	27.9	1.4	
2490-3	9.5305	31.83	104.2502	15.01	−0.465	3	45.8	2.2	46.3	1.7	
2488-6	9.5307	31.84	104.2329	13.97	1.452	3	36.3	2.7	36.8	2.7	
2490-2	9.5307	31.84	104.2488	14.93	−0.311	10	41.9	1.3	41.8	1.5	
2488-4	9.5308	31.85	104.2395	14.37	0.720	1	35.7	NA	36.3	(1.8)	
2490-1	9.5308	31.85	104.2476	14.86	−0.177	3	41.3	0.7	41.2	1.1	
2488-5A	9.5309	31.85	104.2346	14.08	1.264	1	26.4	NA	26.7	(1.5)	
2488-5B	9.5309	31.85	104.2346	14.08	1.264	1	20.6	NA	20.7	(0.1)	
2744-2	9.5562	33.37	104.2490	14.94	−0.111	2	46.1	3.5	48.9	3.4	
2744-1	9.5567	33.40	104.2507	15.04	−0.300	5	40.4	2.6	40.8	2.5	
2352-1	9.5573	33.44	104.2490	14.94	−0.111	7	46.1	2.0	48.4	2.5	
2744-8	9.5581	33.49	104.2485	14.91	−0.054	3	36.7	1.0	36.5	1.3	
2744-7	9.5583	33.50	104.2480	14.88	0.000	9	39.8	1.1	40.3	1.2	
2744-6	9.5587	33.52	104.2478	14.87	0.022	9	43.3	1.6	44.4	1.7	

Table 1. (continued)

Site	Lat, °N	Min Lat	Lon, °W	Min Lon	Dist	N	F_{m1}	σ_1	F_{m2}	σ_2	1991–1992
2494-2	9.5627	33.76	104.2494	14.96	−0.090	3	44.0	1.5	44.1	2.0	
2371-2	9.6027	36.16	104.2502	15.01	0.643	1	45.5	NA	45.1	(0.6)	
2371-4	9.6080	36.48	104.2541	15.25	0.211	2	32.4	0.3	33.1	1.0	
2371-5	9.6083	36.50	104.2544	15.26	0.207	3	35.8	1.6	36.7	2.2	
2371-11	9.6181	37.09	104.2559	15.35	0.011	1	20.7	NA	20.5	(1.6)	
2748-3	9.6452	38.71	104.2576	15.46	0.153	5	39.2	1.1	39.5	1.5	
2748-2	9.6453	38.72	104.2581	15.49	0.098	3	40.5	2.9	40.2	2.6	
2748-1	9.6458	38.75	104.2604	15.62	−0.152	9	38.0	1.1	37.2	1.5	
2748-7	9.6480	38.88	104.2590	15.54	−0.005	3	43.0	1.1	43.4	1.5	
2361-5	9.6520	39.12	104.2605	15.63	−0.055	3	33.7	1.1	34.0	1.4	
2355-4	9.7702	46.21	104.2792	16.75	−0.022	4	33.8	0.5	33.9	0.8	R
2757-2	9.7705	46.23	104.2810	16.86	−0.194	1	34.4	NA	33.4	(4.1)	(R)
2740-6	9.7708	46.25	104.2775	16.65	0.168	3	29.7	2.5	28.7	2.4	R
2740–7	9.7708	46.25	104.2775	16.65	0.168	4	33.3	0.7	32.9	1.2	R
2740-4	9.7717	46.30	104.2774	16.64	0.178	2	40.0	1.1	39.1	2.4	R
2740-1	9.7719	46.31	104.2768	16.61	0.242	5	32.9	0.8	33.5	1.0	R
2360-1	9.7736	46.42	104.2788	16.73	0.022	5	32.6	0.2	32.0	1.0	Y
2360-5	9.7742	46.45	104.2796	16.78	0.011	2	35.9	0.4	36.2	1.2	R
2360-7	9.7747	46.48	104.2798	16.79	0.013	3	33.2	1.6	33.0	1.6	R
2354-V	9.7861	47.17	104.2826	16.96	0.000	3	32.9	0.6	33.2	1.3	R
2502-4	9.7909	47.45	104.2833	17.00	−0.030	8	34.9	1.1	35.0	1.2	R
2370-2	9.7925	47.55	104.2836	17.02	−0.044	1	30.3	NA	30.9	(0.5)	(R)
2502-1	9.7947	47.68	104.2849	17.09	−0.099	4	34.8	0.6	35.1	0.7	R
2502-2	9.7947	47.68	104.2830	16.98	0.111	5	37.0	0.5	36.8	1.6	R
2746-4	9.8154	48.92	104.2882	17.29	−0.025	1	34.7	NA	33.4	(1.1)	(R)
2746-11	9.8155	48.93	104.3020	18.12	−1.549	1	36.8	NA	38.3	(3.4)	
2746-10	9.8157	48.94	104.3004	18.02	−1.371	2	40.6	2.3	40.0	1.7	
2742-4	9.8160	48.96	104.2880	17.28	0.000	3	33.6	1.9	33.8	1.8	Y
2759-5	9.8163	48.98	104.3083	18.50	−2.254	6	41.4	0.7	42.0	1.0	
ARC364	9.8164	48.98	104.3003	18.02	−1.366	2	42.5	1.6	42.7	1.4	
2746-5	9.8165	48.99	104.2885	17.31	−0.050	4	34.2	1.9	34.8	2.0	R
2759-7	9.8165	48.99	104.3095	18.57	−2.377	3	24.2	0.8	24.3	0.7	
2759-2	9.8167	49.00	104.3062	18.37	−2.012	6	42.3	1.3	42.3	1.2	
2746-15	9.8168	49.01	104.3098	18.59	−2.417	3	13.6	0.9	13.4	0.8	
2759-8	9.8169	49.01	104.3103	18.62	−2.472	3	14.3	0.1	13.9	0.3	
ARC374	9.8172	49.03	104.2591	15.55	3.315	3	29.0	0.3	28.9	0.4	
2759-10	9.8179	49.07	104.3129	18.77	−2.753	3	26.5	0.7	26.6	0.8	
2759-12	9.8186	49.12	104.3098	18.59	−2.418	3	23.9	0.6	24.0	0.8	
2759-14	9.8200	49.20	104.3097	18.58	−2.401	1	40.1	NA	40.1	(1.0)	
2760-3	9.8225	49.35	104.3008	18.05	−1.302	2	39.8	0.6	40.8	1.7	
2844-2	9.8232	49.39	104.2888	17.33	0.025	1	36.6	NA	35.6	(3.4)	(Y)
2851-1	9.8232	49.39	104.2880	17.28	0.114	3	32.8	1.2	32.6	2.4	R
ARC480	9.8252	49.51	104.3052	18.31	−1.717	3	45.7	2.6	45.1	2.2	
ARC481	9.8253	49.52	104.3010	18.06	−1.329	2	39.0	0.4	39.7	1.1	
ARC389	9.8254	49.52	104.3126	18.76	−2.609	3	24.8	0.1	24.6	0.4	
2760-6	9.8266	49.60	104.2966	17.80	−0.836	1	34.2	NA	35.2	(3.2)	
3028-2	9.8271	49.63	104.2895	17.37	−0.051	2	34.5	0.3	34.9	1.2	Y
3034-5	9.8272	49.63	104.2892	17.35	0.008	2	36.6	0.6	36.5	1.1	Y
3035-2	9.8295	49.77	104.2895	17.37	0.052	3	38.4	0.9	37.8	0.9	Y
2852-1	9.8301	49.81	104.2891	17.35	0.096	1	33.8	NA	35.6	(5.4)	(R)
2852-2	9.8303	49.82	104.2891	17.35	0.100	4	36.3	1.5	36.7	1.6	Y
2852-3	9.8303	49.82	104.2897	17.38	0.030	1	31.2	NA	31.1	(2.1)	(R)
3031-1	9.8310	49.86	104.2898	17.39	0.018	3	38.1	2.5	38.2	2.5	Y
3029-4	9.8318	49.91	104.2902	17.41	−0.023	1	37.0	NA	37.3	(4.0)	(Y)
3029-5	9.8318	49.91	104.2902	17.41	−0.023	1	40.7	NA	40.5	(2.7)	(Y)
3034-2	9.8319	49.91	104.2901	17.41	−0.015	2	29.5	1.6	29.2	1.4	Y
3023-1	9.8320	49.92	104.2901	17.41	0.000	1	34.1	NA	34.7	(6.3)	(Y)
ARC342	9.8333	50.00	104.3124	18.74	−2.484	3	38.5	0.2	38.6	0.9	
2768-6	9.8334	50.00	104.2727	16.36	2.025	4	37.8	1.9	37.4	1.6	
ARC348	9.8334	50.00	104.2875	17.25	0.377	4	29.6	0.6	29.3	0.8	R
3784-1	9.8335	50.01	104.2744	16.46	1.709	4	36.2	1.3	36.0	1.5	
3784-3	9.8337	50.02	104.2766	16.60	1.470	3	37.4	1.3	37.6	1.2	

Table 1. (continued)

Site	Lat, °N	Min Lat	Lon, °W	Min Lon	Dist	N	F_{m1}	σ_1	F_{m2}	σ_2	1991–1992
3784-2	9.8343	50.06	104.2763	16.58	1.481	3	34.6	1.1	37.1	2.4	
2770-1	9.8354	50.12	104.3000	18.00	−0.997	2	47.3	0.4	47.4	2.6	
3159-1	9.8356	50.14	104.2906	17.44	0.046	2	33.8	1.3	33.1	2.0	Y
3167-2	9.8356	50.14	104.2906	17.44	0.046	2	36.8	3.5	36.4	3.3	(R)
3784-5	9.8361	50.17	104.2767	16.60	1.502	3	35.3	1.7	34.9	1.8	
3784-4	9.8364	50.18	104.2764	16.58	1.546	4	33.7	1.1	33.1	1.2	
2770-3	9.8370	50.22	104.2900	17.40	0.111	1	28.6	NA	28.1	(0.9)	(Y)
2752-6	9.8382	50.29	104.2913	17.48	−0.032	1	36.6	NA	37.6	(5.9)	(R)
3156-1	9.8388	50.33	104.2914	17.48	−0.042	1	39.4	NA	40.2	(0.9)	(Y)
2357-3	9.8389	50.33	104.2911	17.47	−0.011	2	35.5	0.3	34.7	2.9	R
2770-5	9.8390	50.34	104.2900	17.40	0.128	3	36.0	1.5	36.5	1.6	R
3166-1	9.8390	50.34	104.2914	17.48	−0.047	3	31.4	1.9	31.9	2.2	Y
3784-7	9.8409	50.45	104.2773	16.64	1.535	3	49.2	0.8	48.9	0.8	
2734-1	9.8417	50.50	104.2889	17.33	0.340	2	32.8	4.5	33.2	5.0	
3963-6	9.8417	50.50	104.2765	16.59	1.645	2	44.5	1.1	43.5	2.4	
ARC499	9.8419	50.51	104.3172	19.03	−2.898	2	18.9	1.1	19.1	1.4	
2841-1	9.8423	50.54	104.2921	17.53	−0.006	2	36.7	1.7	36.3	4.9	
3963-3	9.8435	50.61	104.2743	16.46	1.916	2	50.7	1.0	50.5	1.4	
2770-7	9.8441	50.65	104.2900	17.40	0.270	5	42.0	2.9	42.9	2.7	
2747-1	9.8444	50.66	104.2951	17.71	−0.340	2	37.5	3.3	38.8	4.3	
2737-1	9.8453	50.72	104.2916	17.50	0.157	2	39.1	4.7	38.0	3.8	
2368-6	9.8487	50.92	104.2937	17.62	0.000	4	37.5	1.8	39.1	3.4	
2737-3B	9.8488	50.93	104.2934	17.60	−0.041	4	36.2	4.5	36.4	4.0	
3163-1	9.8494	50.96	104.2939	17.63	0.000	2	41.8	2.5	41.8	2.4	
ARC320	9.8498	50.99	104.3251	19.51	−3.553	3	14.9	0.9	15.2	0.9	
ARC324	9.8503	51.02	104.3087	18.52	−1.741	1	41.1	NA	41.3	(2.0)	
ARC333	9.8503	51.02	104.2720	16.32	2.442	1	43.8	NA	43.5	(1.1)	
ARC322	9.8505	51.03	104.3175	19.05	−2.713	2	15.8	1.2	15.5	0.9	
ARC387	9.8581	51.49	104.2752	16.51	2.189	1	47.6	NA	48.5	(2.5)	
ARC470	9.8582	51.49	104.2665	15.99	3.156	3	39.7	2.0	40.1	2.2	
ARC465	9.8585	51.51	104.3302	19.81	−4.006	2	7.4	0.4	7.7	0.4	
ARC388	9.8587	51.52	104.2703	16.22	2.735	1	46.7	NA	46.6	(1.2)	
ARC467	9.8588	51.53	104.3218	19.31	−3.082	4	24.6	2.0	24.9	1.7	
2772-6	9.8656	51.94	104.3000	18.00	−0.554	1	38.8	NA	38.9	(1.2)	
2772-5	9.8657	51.94	104.3000	18.00	−0.554	1	34.1	NA	33.6	(1.4)	
ARC315	9.8661	51.97	104.2710	16.26	2.664	2	41.7	0.6	41.8	2.3	
ARC307	9.8668	52.01	104.3038	18.23	−0.971	1	39.8	NA	40.0	(0.3)	
2772-1	9.8669	52.01	104.2745	16.47	2.283	6	47.2	1.7	46.6	1.6	
2772-3	9.8669	52.01	104.2873	17.24	0.853	4	46.3	2.3	46.3	2.0	
2772-2	9.8670	52.02	104.2820	16.92	1.437	2	52.8	2.1	53.3	3.1	
ARC310	9.8670	52.02	104.2919	17.51	0.338	2	37.7	0.1	37.7	0.6	
ARC309	9.8672	52.03	104.2968	17.81	−0.198	3	38.3	0.5	38.2	1.7	
ARC510	9.8711	52.27	104.2963	17.78	0.000	2	38.2	0.3	38.3	1.1	
ARC509A	9.8746	52.48	104.2968	17.81	0.000	2	43.0	2.2	43.3	2.2	
ARC459	9.8753	52.52	104.2698	16.19	2.967	2	52.1	0.7	52.1	1.5	
ARC461H	9.8753	52.52	104.2617	15.70	3.890	6	41.7	2.4	41.9	2.2	
2359-8	9.8823	52.94	104.2983	17.90	0.012	4	42.4	0.7	42.6	0.7	
2497-1A	9.8877	53.26	104.2975	17.85	0.063	2	47.4	0.8	46.9	0.9	
2359-4	9.8879	53.27	104.2978	17.87	0.028	5	35.3	1.3	35.3	1.2	
2497-2	9.8925	53.55	104.2982	17.89	0.067	4	42.6	1.4	43.2	1.8	
2497-3A	9.8941	53.65	104.2982	17.89	0.096	5	38.9	3.0	39.2	2.9	
2497-4	9.8980	53.88	104.2991	17.95	0.065	6	42.0	1.8	41.9	1.6	
2497-6	9.9103	54.62	104.3005	18.03	0.238	3	41.9	0.5	41.5	0.7	
2497-7	9.9217	55.30	104.3030	18.18	0.278	2	39.2	0.4	39.4	1.0	

[a] Abbreviations are as follows: Lat, decimal degrees north; Min Lat, decimal minutes north; Lon, decimal degrees west; Min Lon, decimal degrees west; Dist, distance from axis (km), negative to west; N, number of specimens in site mean; F_{m1}, σ_1, "normal" site mean paleointensity and standard error of the mean (μT); F_{m2}, σ_2, bootstrapped site mean and standard error (see text). Where N = 1, error (in parentheses) is single specimen uncertainty (see text). Under 1991–1992, Y indicates sample believed to be part of the 1991–1992 flow(s) at 9°50'N, R indicates sample near (<500 m) the AST between 9°46 and 50.5'N that may or may not be associated with the 1991–1992 flow but is likely very recent (erupted past 1–2 decades); parentheses indicate that the value is not shown in Figure 9.

resolution bathymetry, and is thought to be related to this event [*Fornari et al.*, 2004].) The timing of this eruption is well constrained by submersible observations [*Haymon et al.*, 1993] and ^{210}Po-^{210}Pb dating [*Rubin et al.*, 1994]. The latter indicates that the eruption occurred in two phases, the first in early 1991, and the second in late 1991 to early 1992. The second phase also appears to have resulted in some fissuring and small flows a few kilometers north of the main flow [*Perfit and Chadwick*, 1998; *Rubin et al.*, 2001].

[12] In contrast to the 9°50′N area, the 9°31′N region is characterized by a wider (100–150 m) AST nested within a larger (~300 m wide), shallow (~10–20 m relief) tectonic graben, suggesting that this portion of the segment is presently less magmatically active [*Fornari et al.*, 1998, 2004]. On the basis of observational and geological evidence, the ages of axial lavas have been estimated at ~500–1000 years by *Haymon et al.* [1991], while at least some flows within the AST have been estimated at <200 years [*Sims et al.*, 2002]. In addition to the well-documented 1991–1992 event at 9°50′N, other recent eruptions in the study area are believed to have occurred between 9°14′and 9°21′ in ~1987–1989 [*Kurras et al.*, 2000; *Fornari et al.*, 2004], and at the small OSC at 9°37′N, possibly related to the 1991 event [*Smith et al.*, 2001].

[13] Numerous seismic studies on the 9°–10°N segment [e.g., *Harding et al.*, 1993; *Vera and Diebold*, 1994; *Christeson et al.*, 1994; *Sohn et al.*, 2004] have found a dramatic increase in seismic layer 2A within ~1–2 km of the axis. Seismic layer 2A is widely interpreted as representing the extrusive pile; in this interpretation, the increase in 2A thickness results from the buildup of the extrusive layer through off-axis eruptions or through channeling axial eruptions onto the flanks of the axial high. It has been further suggested that the thickening of layer 2A correlates with the off-axis extent of lava channel distribution [*Soule et al.*, 2005; *Sohn et al.*, 2004]. Other interpretations suggest that the increase may instead represent a porosity and/or alteration front, unrelated to a lithologic boundary [e.g., *McClain et al.*, 1985; *Grevemeyer et al.*, 1999].

3. Methods

[14] Samples were selected for paleointensity experiments based primarily on a fresh, glassy appearance, and on the strength of their magnetic moment ($> 5 \times 10^{-10}$ Am^2). All specimens were soaked in a dilute (15%) HCl solution to remove any superficial staining. Samples were then packed into glass tubes (1 cm diameter by 3 cm long) with glass microfiber filter paper, and were fixed in place with several drops of potassium silicate. Fiducial lines were etched into the tubes to ensure constant orientation throughout the experiment. Half of the paleointensity experiments were carried out at the paleomagnetic facility at Lamont and half at the Scripps paleomagnetic lab.

[15] We used the stepwise double-heating method of *Thellier and Thellier* [1959], modified by *Coe* [1967], to recover an estimate of the ancient field. We used an applied field of 25 μT, which at Scripps was applied to the samples throughout the entire heating and cooling of the samples during in-field steps. At Lamont, the field was turned on just before the samples were cooled. Samples were heated at 100, 150, and 200°C, then at 25°C intervals until the zero-field magnetization intensity was ≤10% of the natural remanent magnetization (NRM). Thermal alteration of samples was monitored by pTRM checks (repeating a lower temperature in-field step) after every other temperature step.

[16] In addition to the paleointensity experiments, a number of rock magnetic tests were carried out on the samples following the Thellier experiments, primarily to characterize magnetic grain size, which plays a key role in the stability of magnetization in SBG. Low-field susceptibility and a 1 T isothermal remanent magnetization (IRM) were measured on all samples (auxiliary material[1]). Additionally, selected samples were given an IRM (1 T) at liquid nitrogen temperatures, which was measured both before and after warming to room temperature to test for the presence of a superparamagnetic (SP; smaller grain size) fraction. Finally, we carried out hysteresis measurements on chips from these same samples. In addition to the standard hysteresis curve, we also measured the 'saturation initial curve' to calculate the transient energy dissipation [*Fabian*, 2003], or transient hysteresis [*Yu and Tauxe*, 2005].

4. Results

4.1. Magnetic Grain Size and Composition

[17] Submarine basaltic glass is considered an ideal material for paleointensity studies, primarily be-

[1] Auxiliary material is available at ftp://ftp.agu.org/apend/gc/2005gc001141.

cause of the small size of the (titano)magnetite grains, which carry a very stable remanence. Stable single-domain (SD) size grains are required by the Thellier-Thellier paleointensity experiments, as only SD grains satisfy the conditions of independence and reciprocity of partial thermoremanence (pTRM). This means that grains that are demagnetized over a particular temperature interval are also the only grains that are remagnetized during the in-field cooling over the same temperature interval. SD grains have a relatively narrow size distribution, with estimates for pure magnetite ranging from ~25–40 nm (grain diameter) at the superparamagnetic (SP) boundary to 50–84 nm at the transition to nonuniform magnetization [*Dunlop and Özdemir*, 1997]. These estimates are poorly constrained, however, and some evidence suggests that the SP-SD transition may be somewhat smaller [*Tauxe et al.*, 1996; *Lanci and Kent*, 2003].

[18] Magnetic hysteresis data indicate that the grain size in our SBG spans the SP-SD boundary. Clean hysteresis loops were difficult to obtain because of the large paramagnetic contribution, but results are similar to previous SBG data [e.g., *Tauxe et al.*, 1996; *Carlut and Kent*, 2002; *Bowles et al.*, 2005]. Typical loops are shown in Figure 2, and range from specimens with both low H_{cr}/H_c ratios (~1.6) and high M_r/M_s values (~0.5), typical of SD grains (Figure 2a), to loops with varying degrees of constriction, consistent with a mixture of SD and SP grains (or two different magnetic mineralogies) (Figures 2b–2d). Hysteresis parameters are tabulated in Table 2. The degree of constriction in the hysteresis loop can be quantified using the shape parameter (σ_{hys}) of *Fabian* [2003], calculated on the slope-corrected data. σ_{hys} compares the area of the hysteresis loop to that of an ideal rectangle. Values > 0 are reflective of a constricted loop, and increasing σ_{hys} suggests an increasing SP contribution. Figure 2e shows this parameter plotted against the transient energy dissipation ratio (E_t^{Δ}/E_{hys}) of *Fabian* [2003]. This is the ratio of irreversible to reversible self-demagnetization; low values indicate a SD-SP mixture, while high values are typical of multidomain grains. All our samples plot along a mixing trend of SD with various amounts of SP. While a few samples have anomalously high values of E_t^{Δ}/E_{hys}, we suggest this is an artifact resulting from the low signal-to-noise ratio of the ferromagnetic component. This noise makes the parameter especially difficult to calculate accurately, as it requires subtracting two nearly identical branches of the loop.

[19] Results of the low-temperature IRM experiments further support a SD remanence carrier with varying amounts of SP (Figure 3). The loss of low-temperature IRM upon subsequent reequilibration to room temperature is negatively correlated with mass-normalized sample moment (Figure 3). Similarly, samples with high M_r/M_s and σ_{hys} correlate with mass-normalized IRM (positively and negatively, respectively). This is strongly suggestive of a large SP fraction, which decreases with increasing sample magnetization.

[20] We conclude that the grain size of the remanence carrier ranges from stable single domain to grains close to the SD-SP boundary. Such stable SD grains are ideal for paleointensity experiments, while the SP grains do not carry a remanence. Saturation IRM values (auxiliary material) of all samples are strong enough to allow for $\sim 10^8$–10^{10} magnetite grains of SD size (with grain volume approximated by cubes with edge lengths between 25 and 70 nm), which is more than enough to provide a statistical average of the ambient field during cooling.

[21] In most samples the NRM is a single component magnetization that unblocks over a temperature range from ~100°C to 425°C, consistent with fine-grained magnetite or low-Ti titanomagnetite. A clear geographic distinction was observable in the unblocking temperature spectra; samples from within or near the 1991–1992 flow at 9°50′N (9°46′–50.5′, <500 m from the AST) had significantly higher (on average) unblocking temperatures. These samples had an average median destructive temperature (MDT; the temperature required to reduce the remanence to half its initial value) of 385 ± 37°C compared to 295 ± 46°C for all other sites <500 m from the AST, or 301 ± 43°C for all remaining sites regardless of distance from the AST. With this exception, there was little geographic variability in MDT distributions. The high MDTs at 9°50′N could be caused by variations in grain size or, perhaps more likely, Ti content. Interestingly, MDT is inversely correlated to the bulk glass Ti/Fe (r = 0.57), which could suggest a link to ulvöspinel content if the Ti/Fe content of the magnetites is controlled by diffusion processes, as suggested by *Zhou et al.* [2000]. Furthermore, there is no correlation between either MDT or Ti/Fe and any of the grain-size proxies (M_r/M_s, σ_{hys}, low-temperature IRM loss) that might imply a link to grain size variations, though this is based on data from a very small subset of samples. Transmission electron microscopy data

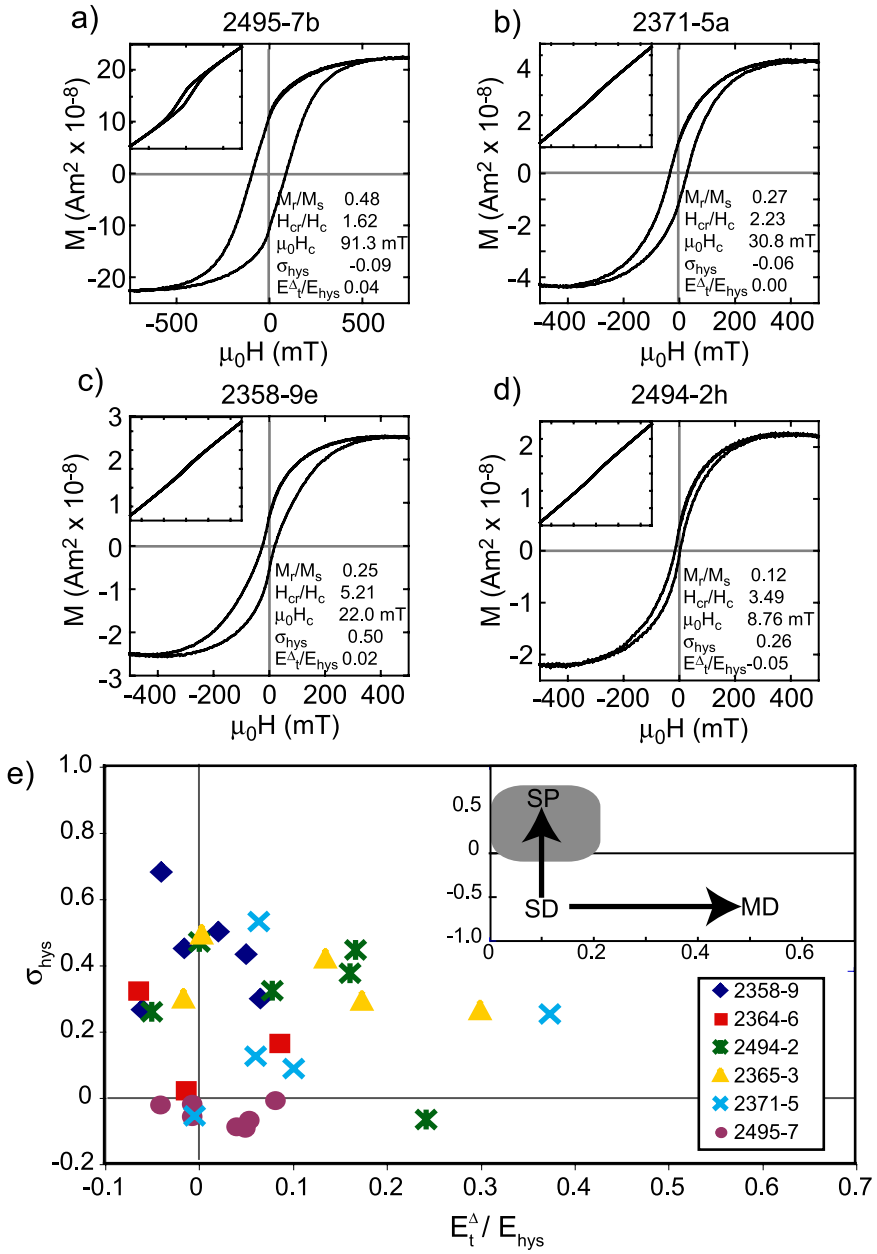

Figure 2. Hysteresis results for glass specimens. (a) and (b) Examples of loops showing predominantly SD-type behavior. (c) and (d) Examples of constricted loops suggestive of admixtures of SD and SP size grains. Maximum field applied was 0.5 T, except for sample 2495-7 (1 T). Insets show loops before paramagnetic slope correction, calculated for H = 75% of maximum. (e) Plot of *Fabian* [2003] hysteresis parameters (see text). Inset shows fields as defined by *Fabian* [2003], and most data from the present study plot in the shaded box, indicating single domain with varying amounts of SP. Negative values for E_t^{Δ}/E_{hys} have no physical meaning and result from the low signal-to-noise ratio of the ferromagnetic component. Similarly, samples with elevated values of E_t^{Δ}/E_{hys} most likely result from noise.

from a significant number of SBG samples might address the relative importance of compositional and grain size variations, but such a study is beyond the scope of the present work. At the least, the correlation between MDT and bulk glass chemistry does suggest that the blocking temperature variations are related to primary magmatic processes, and not to some later seafloor alteration.

4.2. Paleointensity

[22] Most specimens showed ideal behavior in the Thellier experiments, displaying linear plots of

Table 2. Rock Magnetic Results[a]

										IRM Results				
$Sample_1$	F_{anc1}	q	MDT	Whole Sample IRM/Mass	M_r/M_{rs}	H_{cr}/H_c	H_c	E^{Δ}_t/E_{hys}	σ_{hys}	$Sample_2$	Mass	IRM/mass	Whole Sample NRM/Mass	% LT IRM
2358-9a2	40.2	12.3	265.1	5.85	0.21	4.2	14.4	−0.01	0.45	2358-9a	0.0598	5.853	0.169	29
2358-9b2	34.9	34.2	231.6	14.40	0.24	4.4	25.4	0.07	0.30	2358-9b	0.0364	14.396	0.319	24
2358-9d	44.2	17.5	259.4	7.50						2358-9d	0.0555	7.495	0.143	27
2358-9e1	45.1	20.3	255.5	5.32	0.21	4.8	23.5	−0.06	0.26					
2358-9e2	45.1	20.3	255.5	5.32	0.17	6.5	11.1	−0.04	0.68					
2358-9e3	45.1	20.3	255.5	5.32	0.25	5.2	22.0	0.02	0.50					
2358-9e4	45.1	20.3	255.5	5.32	0.12	6.3	12.0	0.05	0.43					
2358-9f	39.0	86.5	192.8	5.33						2358-9f	0.0687	5.328	0.108	37
2364-6a	44.5	26.7	286.5	1.19						2364-6a	0.8790	1.195	0.000	29
2364-6b1	26.0	10.5	291.8	1.59	0.08	9.3	9.3	−0.01	0.02	2364-6b	0.5645	1.593	0.019	39
2364-6b2	26.0	10.5	291.8	1.59	0.16	3.3	15.0	−0.06	0.32					
2364-6c2	40.2	9.3	286.8	1.30	0.06	5.3	5.8	1.04	−0.31	2364-6c	0.5658	1.303	0.014	38
2364-6f1	45.5	36.8	264.7	2.10	0.22	3.4	27.0	0.09	0.17	2364-6f	0.6366	2.105	0.038	35
2365-3b3	35.8	28.5	292.2	2.02	0.06	11.4	5.9	0.17	0.29	2365-3b	0.5779	2.025	0.044	36
2365-3b4	35.8	28.5	292.2	2.02	0.08	6.5	6.1	0.00	0.49					
2365-3e1	35.3	42.6	303.0	1.58	0.15	6.0	17.0	−0.02	0.30	2365-3e[b]	0.6096	1.788	0.039	40
2365-3e2	35.3	42.6	303.0	1.58	0.10	9.0	9.3	0.30	0.26	2365-3e[b]	0.0744	1.505		56
2365-3Xb	33.7	28.8	288.3	2.42						2365-3Xb	0.8317	2.417	0.057	31
2365-3Xe2	34.4	63.8	294.3	2.35	0.16	6.7	15.6	0.14	0.42	2365-3Xe	0.7276	2.350	0.057	29
2371-5a1	33.7	41.3	225.6	8.91	0.17	5.0	19.4	0.10	0.09	2371-5a	0.2245	8.909	0.209	31
2371-5a2	33.7	41.3	225.6	8.91	0.27	2.2	30.8	0.00	−0.06					
2371-5a3	33.7	41.3	225.6	8.91	0.34	2.4	40.5	0.06	0.12					
2371-5b1	35.0	21.7	244.0	3.87	0.20	4.6	16.7	0.06	0.53	2371-5b	0.1640	3.872	0.091	38
2371-5b2	35.0	21.7	244.0	3.87	0.13	4.7	9.6	0.38	0.25					
2371-5c	38.8	25.7	316.5	1.19						2371-5c	0.4947	1.195	0.023	39
2494-2a	28.0	13.0	360.6	1.00						2494-2a	1.0733	0.997	0.012	38
2494-2f1	44.6	32.7	358.3	4.07	0.15	5.6	13.4	0.17	0.44	2494-2f	0.4322	4.072	0.099	42
2494-2f2	44.6	32.7	358.3	4.07	0.21	4.2	23.2	0.08	0.32					
2494-2g1	41.1	24.0	371.1	5.09	0.10	2.5	12.4	0.24	−0.07	2494-2g[b]	0.1727	2.860		55
2494-2g2	41.1	24.0	371.1	5.09	0.17	5.1	10.4	0.00	0.47	2494-2g[b]	0.1532	7.441		67
2494-2g3	41.1	24.0	371.1	7.44	0.15	6.8	12.9	0.16	0.37					
2494-2h1	46.2	45.7	344.4	3.69	0.12	3.5	8.8	−0.05	0.26	2494-2h	0.3168	3.693	0.090	31
2495-7a2	8.2	38.8	326.4	99.25	0.51	1.5	96.4	−0.01	−0.06	2495-7a	0.0667	99.250	0.555	17
2495-7b1	7.8	37.8	312.5	223.90	0.48	1.6	91.3	0.04	−0.09	2495-7b	0.0318	223.899	1.142	20
2495-7b2	7.8	37.8	312.5	223.90	0.52	1.5	97.9	0.05	−0.07					
2495-7c1	7.7	36.1	321.8	156.17	0.50	1.5	97.7	0.05	−0.09	2495-7c	0.0324	156.173	0.815	22
2495-7c2	7.7	36.1	321.8	156.17	0.44	1.8	83.7	0.08	−0.01					
2495-7d1	8.0	68.9	273.4	119.89	0.50	1.6	96.9	−0.04	−0.02	2495-7d	0.0362	119.890	0.599	29
2495-7d2	8.0	68.9	273.4	119.89	0.48	1.7	91.3	−0.01	−0.02					

[a] Abbreviations are as follows: $Sample_1$, number following sample name refers to separate chips from same sample used for hysteresis experiments; F_{anc1}, sample paleointensity (μT), corresponds to F_{anc1} in the auxiliary material; *q*, quality factor [*Coe et al.*, 1978]; MDT, median destructive temperature (°C); Whole Sample IRM/Mass, mass-normalized IRM ($\times 10^{-4}$ Am^2 kg^{-1}); M_r/M_{rs}, remanent magnetization/saturation magnetization; H_{cr}/H_c, coercivity of remanence/coercivity; H_c, coercivity (mT); E^{Δ}_t/E_{hys}, transient energy dissipation ratio [*Fabian*, 2003]; σ_{hys}, shape parameter [*Fabian*, 2003]; $Sample_2$, IRM experiments performed on whole sample; Mass, sample/split mass (g); IRM/Mass, sample/split mass-normalized IRM($\times 10^{-4}$ Am^2 kg^{-1}); Whole Sample NRM/Mass, mass-normalized NRM($\times 10^{-4}$ Am^2 kg^{-1}), not available for split samples; and % LT IRM, percent low-temperature IRM lost (see text).

[b] Samples that inadvertently split into two, allowing experiments on both splits.

NRM lost versus pTRM gained (Arai plots; Figure 4). Additionally, most samples show no evidence of alteration during the experiment below 400°–450°C, as evidenced by the reproducibility between two in-field measurements at a given temperature (pTRM check). The absence of growth of a new magnetic phase is also attested to by the fact that the zero-field steps of most specimens have a remanence that decays to the origin of a vector endpoint diagram (Figure 4, insets). This is measured by the angle (α) between the principal component of the selected interval (anchored at the center of mass of the data) and the vector average of the data (anchored at the origin) [*Selkin and*

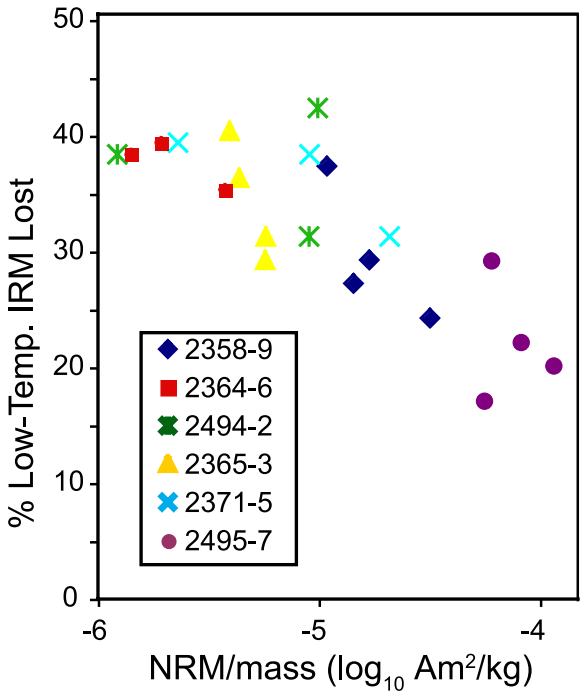

Figure 3. Results of low-temperature IRM experiments. Percent of low-temperature (−196°C) SIRM lost on warming to room temperature, plotted against mass-normalized NRM.

Tauxe, 2000]. Significant alteration via growth of new magnetic minerals should be accompanied by displacement of the remanence into the applied field direction.

[23] The overall quality of the data appears to be linked to sample moment. One measure of quality in the Thellier experiment is the quality factor (q) as defined by *Coe et al.* [1978]. This factor takes into account the scatter of points about the best fit slope, as well as the fraction of NRM (f) used to determine the slope, and a measure of the uniformity in spacing of points along the slope (gap factor, g). Weaker samples (NRM < 10^{-9} Am^2) often result in lower-quality data (low q values; Figure 5), typically manifested in a scattered Arai plot (e.g., Figures 4e–4f). This is further reflected in within-site scatter; sites with high mean q typically have a lower standard deviation of the site mean, while sites with a low mean q may have widely varying standard deviations. We note measurement reproducibility on the Scripps magnetometer is ~$1–3 \times 10^{-11}$ Am^2. So a sample with an initial NRM of 1×10^{-9} Am^2 that has been demagnetized to 10% of the NRM might have a 10–30% measurement error in the final, high-temperature steps, leading to scatter in the Arai plot. For samples with lower initial moments, this effect would be greater.

[24] Although nearly a third of our SBG specimens had NRMs < 10^{-9} Am^2, we chose fairly stringent acceptance criteria for specimens to be included in a site mean: (1) the magnetization must be single component; (2) the NRM-pTRM plot must not show obvious curvature; (3) α must be <10°; and (4) to ensure sufficient reproducibility between two in-field measurements at a given temperature, the difference between repeat in-field steps normalized by the length of the selected NRM-pTRM segment must be less than 5%. A final critical factor in determining paleointensity is the temperature interval over which the slope determination is made. Slopes were picked starting (at T_{min}) either when the sample started unblocking, or after removal of any low-temperature viscous overprint. The latter was typically achieved by 150°C, in accordance with calculations of thermoviscous magnetization [*Pullaiah et al.*, 1975; *Stacey and Banerjee*, 1974] which predict that laboratory temperatures between 100° and 150°C for 30 min. will remove a viscous remanence acquired at 2°C over 40 kyr or at room temperature over 5–10 years (the storage period of most of our samples). The maximum temperature (T_{max}) included in the slope calculation was the highest step that still passed pTRM checks or the step by which <10% of the NRM remained.

[25] After applying these acceptance criteria and picking the slopes as outlined above, 551 specimens remain out of 919 total, with no systematic differences between specimens processed at Scripps and those processed at Lamont. Of these remaining specimens, the mean quality factor (q) is 37 (max = 208; min = 5.4). The distribution of values for q, as well as for α, f, and the pTRM check are shown in Figure 6, both before and after applying the selection criteria. These parameters are tabulated in the auxiliary material. We note that many specimens fail the pTRM test (number 3 above) not necessarily because they are altering during the experiment, but because of the noise inherent to the low-intensity samples. However, we felt it was important to enforce this strict pTRM cutoff to ensure we are not including samples that may be growing a magnetic phase at high temperatures, as this could result in an underestimate of the field.

[26] Site means and standard errors were calculated both in the conventional manner, and by using a bootstrap analysis as by *Bowles et al.* [2005]. In the

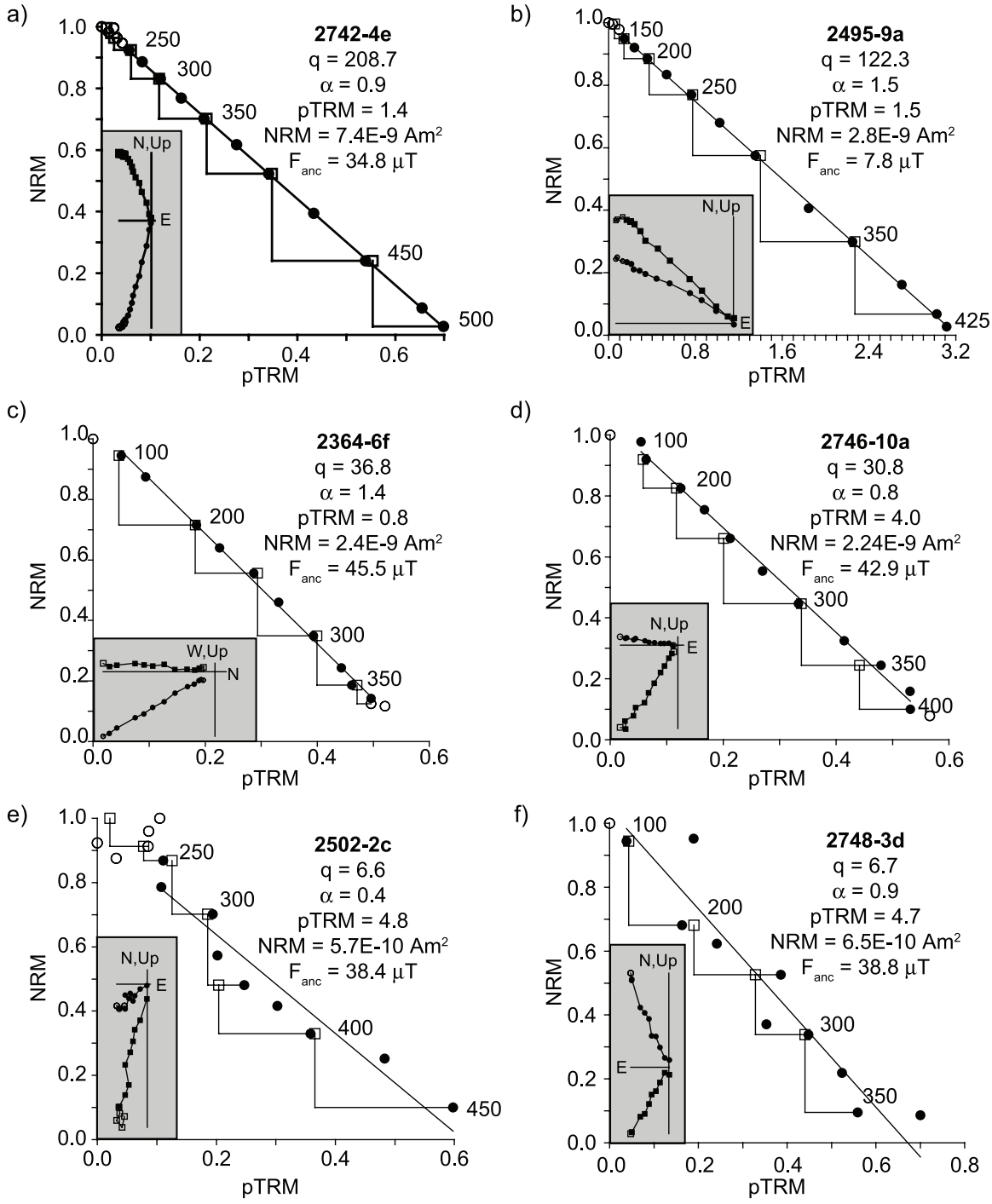

Figure 4. Representative NRM-pTRM plots. All values are normalized by the original NRM. Solid circles represent points used in calculation of the shown best fit slope. These are also the points that are used to calculate the "average" slope and standard deviation (see text). Squares are pTRM checks. Selected temperatures shown in degrees Centigrade. (inset) Vector endpoint diagrams showing demagnetization behavior of samples. Vertical projection in circles; horizontal projection in squares.

latter case, uncertainties at the specimen level were estimated by calculating slopes for all possible combinations of four or more points between T_{min} and T_{max}, subject to the requirement that if a selection of points fails a looser pTRM test (pTRM > 10%) or comprises less than 50% of the NRM ($f < 0.5$), we exclude this subset of points. Site mean results are tabulated in Table 1 and are shown

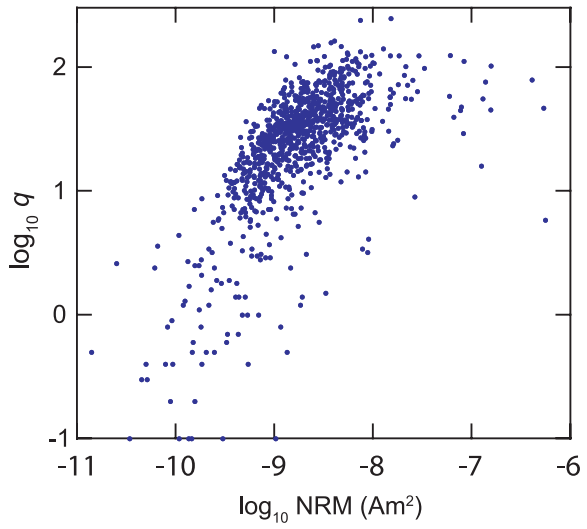

Figure 5. NRM versus quality factor, q [*Coe et al.*, 1978]. Samples with low magnetic moment tend to result in less reliable paleointensity results. Data from all specimens are shown, and slopes were automatically picked using the set of points that would maximize q.

in map view in Figure 7. In Figure 7, and for the remainder of the paper, we use the bootstrapped means with their associated standard errors, which typically provide a more conservative error estimate (Table 1). Note that some site "means" are estimates from a single specimen, and in this case the error (shown in parentheses in Table 1) is the specimen uncertainty described above. However, in many cases these single-specimen site means are corroborated by additional specimens that failed one of our acceptance criteria; of the 33 sites listed in Table 1 with N = 1, 21 have additional specimens that failed the pTRM check criteria, most with pTRM values of 5–10%. For 14 of these 21 sites, the second (and/or third) specimen agrees with the first to within 10% of the paleofield value.

5. Discussion

[27] Paleointensity values range from 6.5 to 53.3 μT and the pattern about the ridge axis is similar to that expected from independent estimates of geomagnetic intensity variation. Global compilations of archeomagnetic and volcanic data indicate that the field experienced a major intensity low at 40 ka (the Laschamp excursion) where the field was <20% of its present value [e.g., *Roperch et al.*, 1988]. On average, the field then increased to values significantly (~40–50%) higher than today's value at ~1–3 ka. Since this time, the field

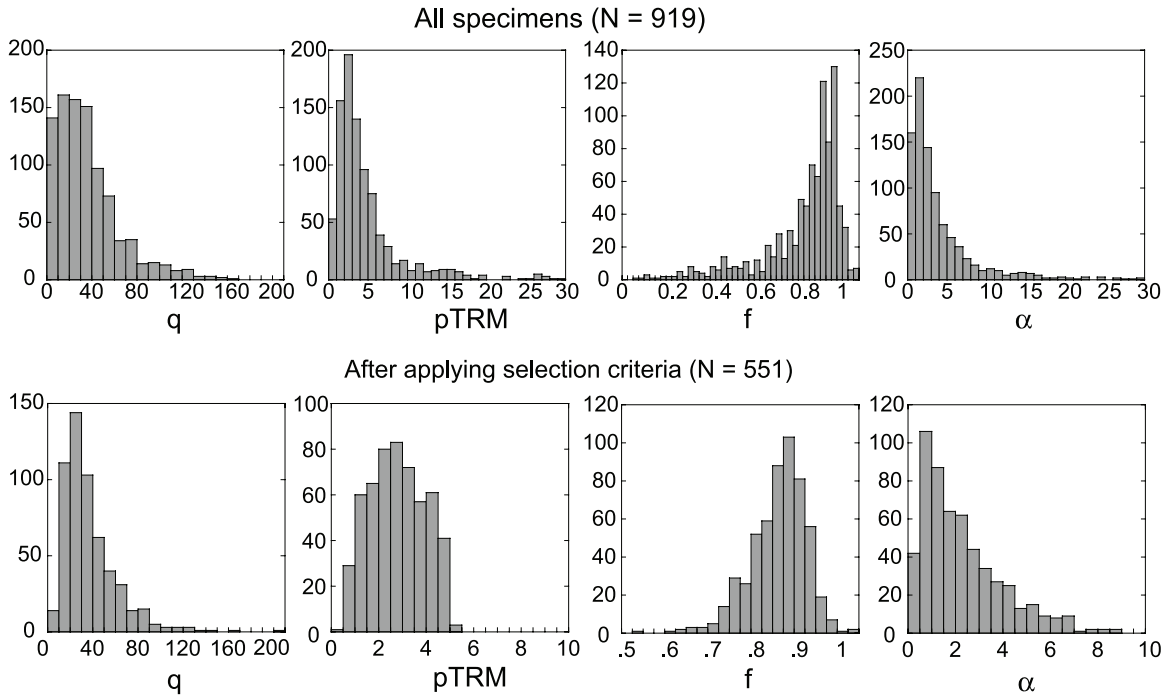

Figure 6. Histograms of parameters describing paleointensity data set (see text). (top) Parameters for unfiltered data set. All samples subjected to paleointensity experiments are included, and parameters were calculated automatically by finding the set of points that maximized q. Note that the horizontal scale for both pTRM and α have been truncated at 30. (bottom) Parameters for final data set used in calculation of site means. Requirements include $\alpha \leq 10$ and pTRM ≤ 5. Note that both horizontal and vertical scales are different from top plots.

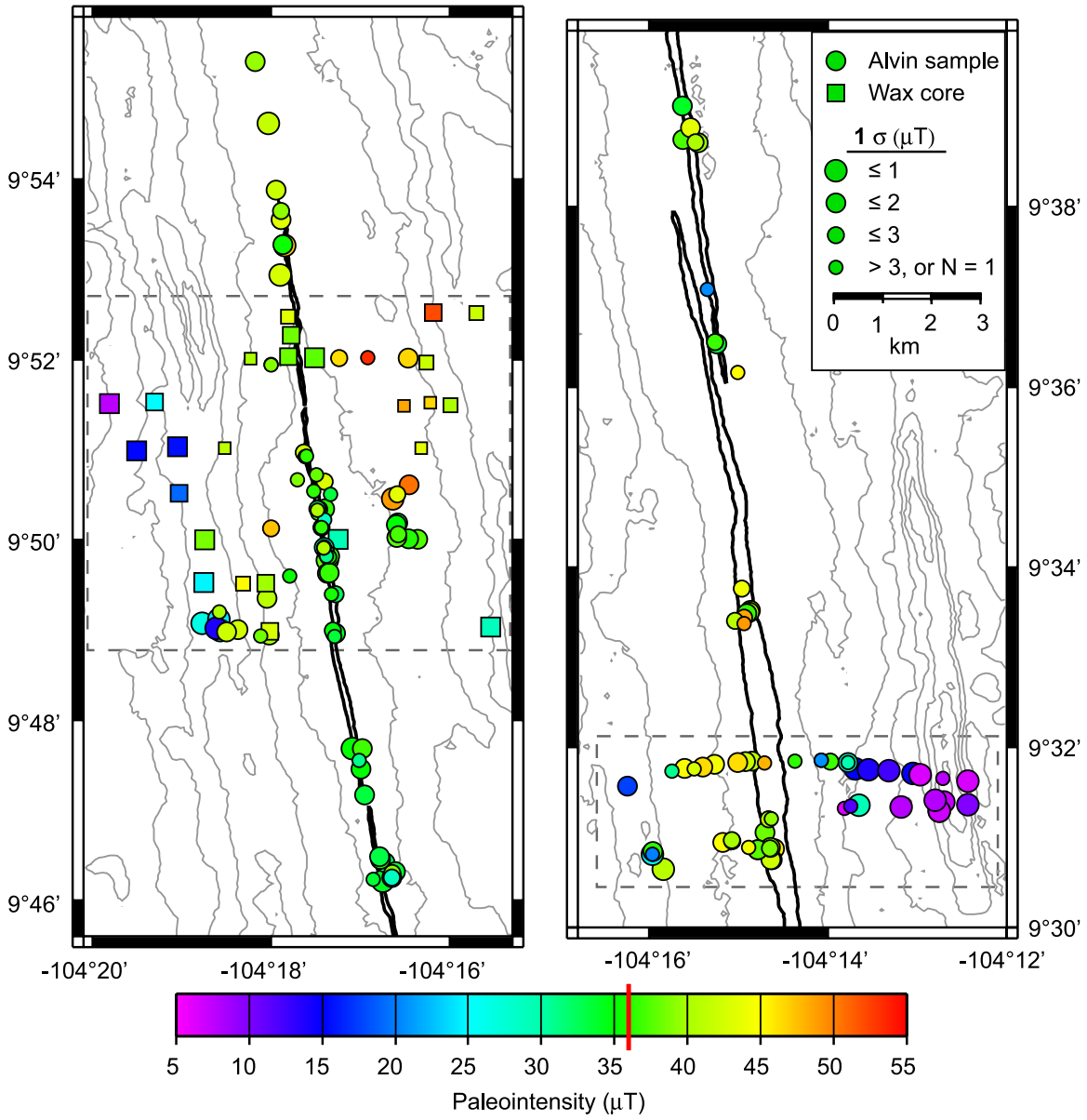

Figure 7. Results of paleointensity experiments. Intensity is indicated by color (see also Table 1). The 1991 field intensity at the site was 35.8 μT, as indicated by red bar on color scale. Circles represent samples collected via *Alvin* submersible, and squares represent samples collected via rock core. Size of symbol corresponds to uncertainty in the site mean. Heavy black line is outline of axial summit trough. Gray lines are 50 m bathymetric contours [*Cochran et al.*, 1999]. Note that closed contours running north-south along ~104°12–13′W enclose a topographic depression. Dashed line boxes show areas depicted in Figures 11 and 12.

has been (on average) decreasing to the present value. The paleointensity data reflect these trends, with near-present-day values along the AST, flanked by values higher than present-day out to ~2 km from the AST, then falling to values significantly lower than present-day on the oldest crust sampled (based on spreading rate) at ~2–4 km. These trends have been seen previously in the much smaller data set of *Mejia et al.* [1996], and it should be noted that in cases where we duplicated their samples (primarily near 9°31′N), our results are nearly identical to those of *Mejia et al.* [1996].

[28] Of course, field behavior is much more complex than this simple picture, and with local deviations from a global average. Because part of this study is aimed at evaluating the use of paleointensity as an age constraint, we need to examine known variations in field intensity a bit more closely.

5.1. Models of Paleofield Variations

[29] In order to use paleointensity as a temporal marker to place age constraints (relative or absolute) on samples or flows, we need a reasonable idea of how the field intensity has changed over the past 40–60 kyr. Our ability to use paleointensity as a dating tool decreases significantly with age of the sample, both because our knowledge of field behavior is less well constrained, and because field intensity is a nonunique function of time. However, there are certain sufficiently unique characteristics of the field over certain time intervals that allow us to place some age constraints. As mentioned above, we know that the field experienced a major low intensity at 40 ka and a high at ~1–3 ka [e.g., *Yang et al.*, 2000] before decreasing to present-day values.

[30] It is this most recent time interval, the past few hundred years, that holds the greatest potential for use in dating young mid-ocean ridge flows. As a model for very recent variation in paleointensity, we start with the IGRF since 1990 and then use the historical field model of *Jackson et al.* [2000] back to 1850. This model (known as gufm1) is shown in Figure 8a (inset), evaluated at a central location in the study site. By comparison with geomagnetic observatory data in Honolulu, Hawaii, and Fresno, California, the model misfit between 1900 and 1990 is on the order of 200–350 nT, with the model intensities higher than the observed. A similar comparison to Huancayo, Peru, data shows a smaller misfit of about −60 to +80 nT. While the model uncertainty is likely to be somewhat greater at our study site, which is constrained by fewer data, the error is likely to be <1 μT, which is less than the 2σ uncertainty in most of our paleointensity estimates. Prior to 1840, no direct observations of field intensity exist, and the *Jackson et al.* [2000] model is constrained only by directional data and assumes a linear decay in the dipole term based on extrapolation of data from more recent time periods. For our purposes therefore we don't directly compare sample paleointensities to this portion of the curve; rather, we turn to archeomagnetic data to get a general idea of field behavior for time periods between ~150 and 5000 ybp.

[31] A global archeointensity curve (Figure 8a) [*Yang et al.*, 2000] suggests a broad peak in intensity lies between about 3500 and 1000 ybp (based on 2912 data points in the 0–5 kyr interval). A more recent compilation by *Korte and Constable* [2005] shows similar variation. However, these globally averaged data sets are heavily weighted

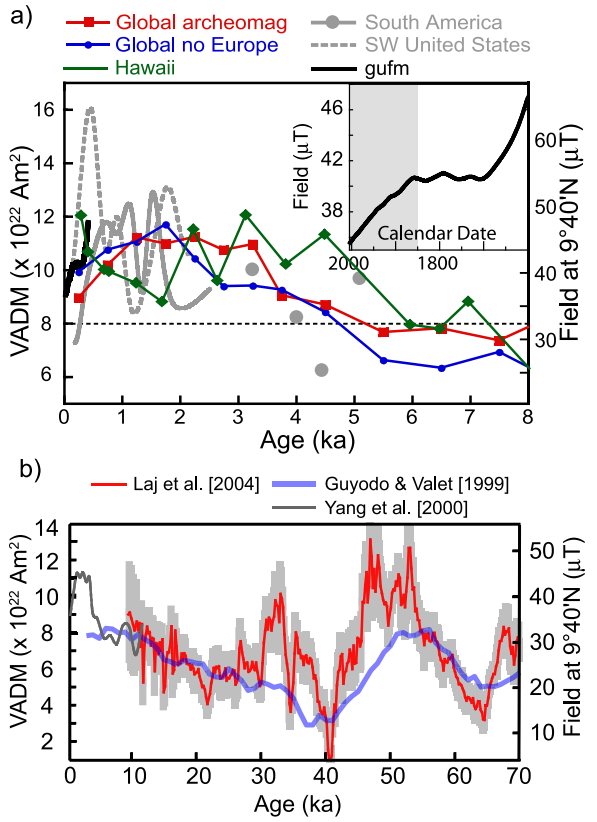

Figure 8. (a) Archeomagnetic data for the past several thousand years. Globally binned and averaged data of *Yang et al.* [2000] shown in red squares, and in blue circles is shown the same curve minus European data. Regional data from northwestern South America and southwestern U.S. from the compilation by *Bowles et al.* [2002] shown in gray solid and dashed lines, respectively. Lines are a splined fit to data averaged in 200 year bins. Solid circles represent single data points. Hawaiian volcanic data of *Mankinen and Champion* [1993a] are in green diamonds; ^{14}C ages are calibrated using CALIB v5.0 [*Stuiver and Reimer*, 1993] with data from *Reimer et al.* [2004]. The gufm1 model of *Jackson et al.* [2000] was evaluated at 9°40′N on the axial summit shown in bold black line and in inset. Shaded area is the portion of the curve directly constrained by intensity data. Dashed horizontal line is present-day global average VADM. (b) Two stacked sedimentary records of paleointensity variation: the SINT800 record [*Guyodo and Valet*, 1999] and a higher-resolution stack, dominated by records from the Atlantic [*Laj et al.*, 2004]. Also shown is the global archeomagnetic curve [*Yang et al.*, 2000].

toward Europe, and the same data set [*Yang et al.*, 2000] without the European data (N = 1002) shows a peak somewhat shorter in duration (~2500–500 ybp) outside of Europe. Furthermore, secular variation on the local scale can result in significant departures from these broad trends that must be

taken into account if possible. An examination of the data sets closest to the study site suggests that the field behavior may be slightly more complex. A compilation of archeomagnetic data from the southwest United States (N = 58) and northwest South America (N = 42) [*Bowles et al.*, 2002] suggests that the high may not have begun until ~2000–1500 ybp, and may have persisted until as recently as 500 ybp, with a short-term drop to near present-day values around 1500–1000 ybp (Figure 8). Volcanic data from central and southern Mexico, after being subjected to some relatively loose quality control standards, suggest that the field increased to high values in that region sometime between 4000 and 2000 ybp [*Morales et al.*, 2001]. Mexican data from *Böhnel et al.* [1997] also support high values at ~1700 ybp. Volcanic data from Hawaii, much more numerous yet significantly farther from the study site, suggest that the increase to high field values may have begun as early as 5000 ybp at that location [*Mankinen and Champion*, 1993a, 1993b; *Laj et al.*, 2002; *Teanby et al.*, 2002]. Finally, a global spherical harmonic model similar to that of *Jackson et al.* [2000] (see above), but based on paleomagnetic rather than historical data for past 7 kyr [*Korte and Constable*, 2005] can be evaluated at the study site. While the pattern of variation is similar to that indicated by the South American data set (Figure 8), the intensities are significantly lower than would be predicted by any of our regional reference curves, with maximum values of 40–42.5 μT, compared to the maximum of 53 μT in the present SBG data set.

[32] The point of examining these regional data sets is not to generate a specific curve to which we can match our new paleointensity data, but to estimate trends in field behavior. In this way, we can estimate the probability, for example, that a sample with high values is associated with a certain time interval. While it may not be strictly appropriate to use any of these data sets which are at significant distances from the study site, until a local secular variation curve can be constructed for 9°–10°N, these are the best data available for estimating general trends. Because the study site lies between the data sets from the Americas which roughly agree with each other, we will assume that paleointensities significantly higher than present-day were most likely erupted between ~500 and 2000 ybp (possibly as old as 4000 ybp) and that for the period <500 ybp field values in this region were most likely decreasing, on average. While this decrease is not likely to be monotonic at all locations, we suggest that over this time interval it is probable that a sample with a higher paleointensity is older than a sample with a lower paleointensity.

[33] In addition to the high values at 500–2000 ybp, another unique feature in paleointensity variations over the past 100 kyr is the low associated with the Laschamp excursion at ~40 ka. This extreme low (<20% of today's value) appears to be a global feature, found in volcanic records in France [*Roperch et al.*, 1988] and Iceland [*Levi et al.*, 1990], as well as in sedimentary paleointensity [e.g., *Guyodo and Valet*, 1999; *Laj et al.*, 2004] and cosmogenic isotope [e.g., *Beer et al.*, 2002; *Frank et al.*, 1997] records. Recent new K-Ar and $^{40}Ar/^{39}Ar$ dating of the type section in Laschamp, France gives concordant ages of 40.4 ± 2 ka (2σ) [*Guillou et al.*, 2004]. The duration of this excursion has been estimated to be ~1500 years on the basis of North Atlantic sediment cores tied to the GISP2 age model [*Laj et al.*, 2000]. In general, however, the intensity low appears to be somewhat broader than the directional excursion associated with it [e.g., *Laj et al.*, 2000; *Lund et al.*, 2005], but the very low values most likely do not last longer than a few thousand years.

[34] Other relative lows in the paleointensity record have been observed. Notably, a low somewhere between ~30 and 35 ka (often called the Mono Lake excursion) and possibly one at ~20 ka are seen in sediment records [e.g., *Laj et al.*, 2004], field reconstructions from ^{36}Cl data [*Beer et al.*, 2002], volcanic absolute paleointensity from Hawaii [*Laj et al.*, 2002] and possibly from Amsterdam Island in the Indian Ocean [*Carvallo et al.*, 2003]. In none of these records are the extreme low intensities of the Laschamp matched. However, it should be noted that if one of these younger events were very short in duration, the full extent of the intensity anomaly would be smoothed in the sediment record. So while it is possible that some very low values may have been achieved after the Laschamp, there is no evidence that this could have happened at times younger than 20 ka.

[35] To summarize the paleofield constraints we use in the interpretation of our SBG data, for times <150 ybp, we utilize the IGRF and the gufm1 model of *Jackson et al.* [2000]. For times <500 ybp, we assume the field has on average been decreasing. We equate paleointensity values significantly higher than the present-day field (~36 μT) with the paleofield high at ~500–2000 ybp. Moderately low paleointensities (<20 μT) we assume are "old", probably > 20 ka. Finally, very low paleo-

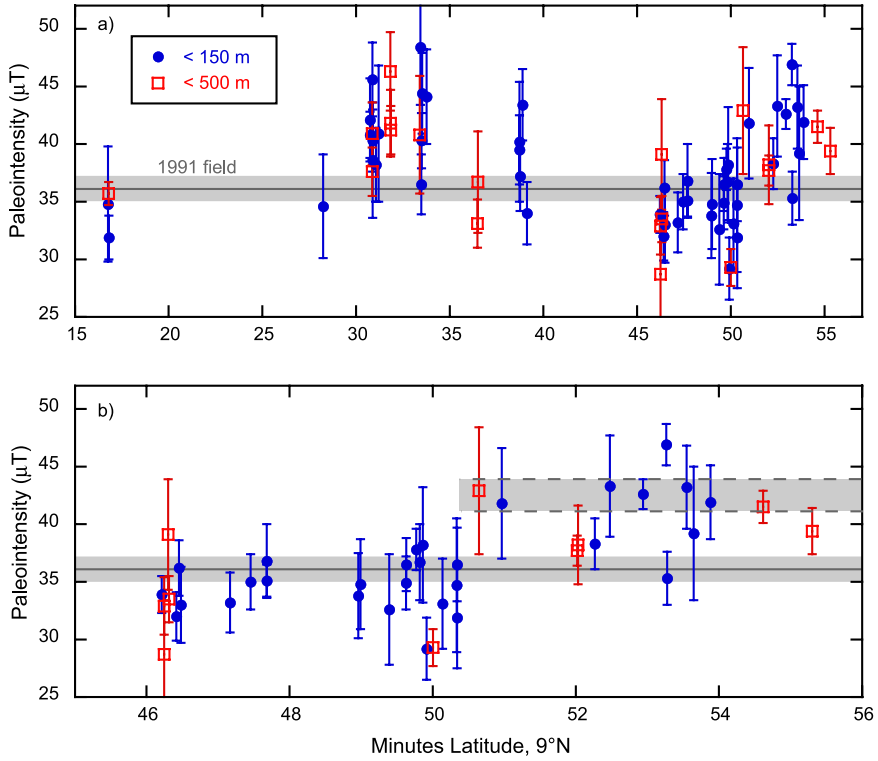

Figure 9. (a) Paleointensity of axial samples plotted against latitude (minutes at 9°N). (b) Enlargement of region between 9°45 and 56′N. Blue circles are samples located <150 m from the center of the AST. Red squares are samples <500 m from the AST. Data shown are bootstrapped site means, and error bars represent the 95% (2σ) uncertainty of the mean. Sites with only one specimen (N = 1) or with a standard error (1σ) > 3.0 μT are not shown. Solid gray horizontal line represents the field intensity at 9°40′N in 1991. Shaded area with dashed bounds indicates field intensity during a possible period of extensive eruptive activity ≥∼150 ybp (see text).

intensity values (<8 μT) are most probably associated with the Laschamp excursion, but we can't preclude the possibility that they may be as young as 20 ka.

5.2. Along-Axis Observations

[36] We restrict our initial analysis to samples located within 500 m of the center of the AST, which may be most suitable for absolute dating by comparison with field models or regional data. In this region of extensive volcanic collapse and glassy lobate and sheet lava, observational evidence supports eruption ages of much less than 1 ka, a time period during which we suggest the field has been predominantly decreasing. Figure 9 shows paleointensity for samples located <500 m from the AST plotted as a function of latitude along axis, with samples at <150 m shown separately with circles. We have further restricted the data shown to those with bootstrap standard errors (1σ) <3.0 μT. We immediately see that some portions of the axis have paleointensities significantly higher than others, representing older regions. Specifically, the region between 9°30′ and 9°32′N is dominated by higher paleointensities, consistent with observations that this portion of the ridge has not recently been as volcanically active as other areas [e.g., *Fornari et al.*, 1998]. Likewise, the area north of ∼9°50′N is characterized by elevated paleointensity values, which is corroborated by dive observations of older looking terrain compared to the area immediately to the south. This latter section to the south (between ∼9°46 and 9°51.5′N) is the locus of the 1991–1992 flow(s) and the observed near present-day values are expected. Similarly, samples at ∼9°17′N and 9°37′N (locations also thought to have experienced flows in the past 2 decades), as well as at 9°28′N, have paleointensities that overlap the hypothesized eruption dates at the 95% confidence level.

5.2.1. A Test of Absolute Dating

[37] A true test of this dating method lies in a closer examination of the samples from the 1991–1992 flow area (Figure 9b). If all of the samples

between 9°46 and 9°51′N were erupted during the 1991–1992 event, we expect them to be consistent with the field at that time (IGRF-10; shown as a horizontal line). While the majority of the samples overlap that value, a significant fraction falls below the 1991 field at the 95% confidence level. Most of these have mean paleointensities that differ from the expected vale by <10%, but a few differ by up to ~20%. Although the field intensity continued to decline after 1991–1992, these low values cannot be explained by an undetected eruption after 1992, as all of these samples were collected before 1996, when the field was 36.0 μT. There remain several possible explanations for these low values: (1) the samples are not part of the 1991–1992 flow, but are older and not covered by younger flows; (2) local field variations due to a magnetic terrain effect are significant; (3) some process is introducing bias during the paleointensity experiments; and (4) at least some of the SBG is not recording or preserving a primary thermoremanence. We discuss each of these possibilities in turn below.

[38] Our current knowledge of field behavior suggests that the last time the field was lower than present-day values was at least 1 ka, but probably 2–4 ka. Therefore, if these samples are older, they must either be significantly older, or our knowledge of recent field behavior is incomplete. The freshness of the samples, their location within or directly adjacent to the AST, and their geochemical similarity to the dated samples from the 1991–1992 event argue against the former. Accurate satellite mapping of the field since the 1970s implies that field models should be reliable for at least 30 years, and it seems unlikely that these low values can be explained by calling on an older age.

[39] A more likely possibility is the existence of significant local field variations due to a magnetic terrain. Near-bottom magnetic data near 9°50′N suggest that anomalies over the AST are consistently negative, and are on the order of ~200 nT (not reduced to pole) at an altitude of ~40 m [*Schouten et al.*, 1999, 2002; *Fornari et al.*, 2004]. Closer to the bottom, these anomalies will be significantly greater, but anomalies of up to 5–6 μT would be required to explain some of the paleointensity values. Simple forward calculations (adapted from *Blakely* [1996]) of a 2-D trough structure intended to approximate the shape and orientation of the AST at 9°50′N show that within the trough the anomaly measured at 2 m above the floor will be consistently negative with an intensity of ~500 nT in the trough center (Figure 10a). Much higher values (up to 2–5 μT) can be achieved close to the trough walls. This result is relatively insensitive to reasonable variations in direction and intensity of the magnetization, trough depth, and angle of the wall slope. Results from three-dimensional modeling (adapted from *Blakely* [1996]) on high-resolution ABE Imagenex ABE microbathymetry [*Fornari et al.*, 2004] near 9°50′N suggest that deviations from the ideal 2-D case can easily produce positive, as well as negative, anomalies. The anomaly generated at 10 m above the bathymetry (Figure 10b) shows that negative anomalies predominate on the trough floor and western trough wall, with amplitudes up to ~1 μT (Figure 10b). However, the eastern trough wall is characterized predominantly by positive anomalies. It should also be noted that east-west striking features (such as the channel in Figure 10b) hold the potential to generate much larger anomalies at this location than the north-south striking trough. We also calculated the anomaly at 2 m above the bathymetry (Figure 10c) for a smaller area indicated by the dashed box in Figure 10b. At this elevation, the anomaly pattern is very similar to that at 10 m, but the amplitude of the anomalies is somewhat larger (up to 3–4 μT in places). Although it is impossible to determine what the field was at a given location when a flow was quenched, it is clear that some of the complicated and extreme topography found within the AST can produce significant anomalies. It is less clear that these anomalies will have a negative bias, although that may be true of samples collected from the trough floor. It is also important to note that the horizontal resolution of the bathymetry is ~5 m, so anomalies generated by features smaller than this are not represented here.

[40] Because the terrain effect should at least sometimes produce positive anomalies, we must also consider that some process is introducing bias during the paleointensity experiments. Cooling rate has previously been examined as a source of bias in field estimates from SBG by *Bowles et al.* [2005], where it was initially suspected that slower laboratory cooling (compared to the natural quench rate) might produce a negative bias in the paleointensity estimates. However, results of this study found that a consistently negative bias was unlikely [*Bowles et al.*, 2005]. In the present case, however, samples from the 1991–1992 flow area have significantly elevated unblocking temperatures. This results in relatively higher natural cooling rates compared to other samples, as cooling rate decreases with temperature because of the decreas-

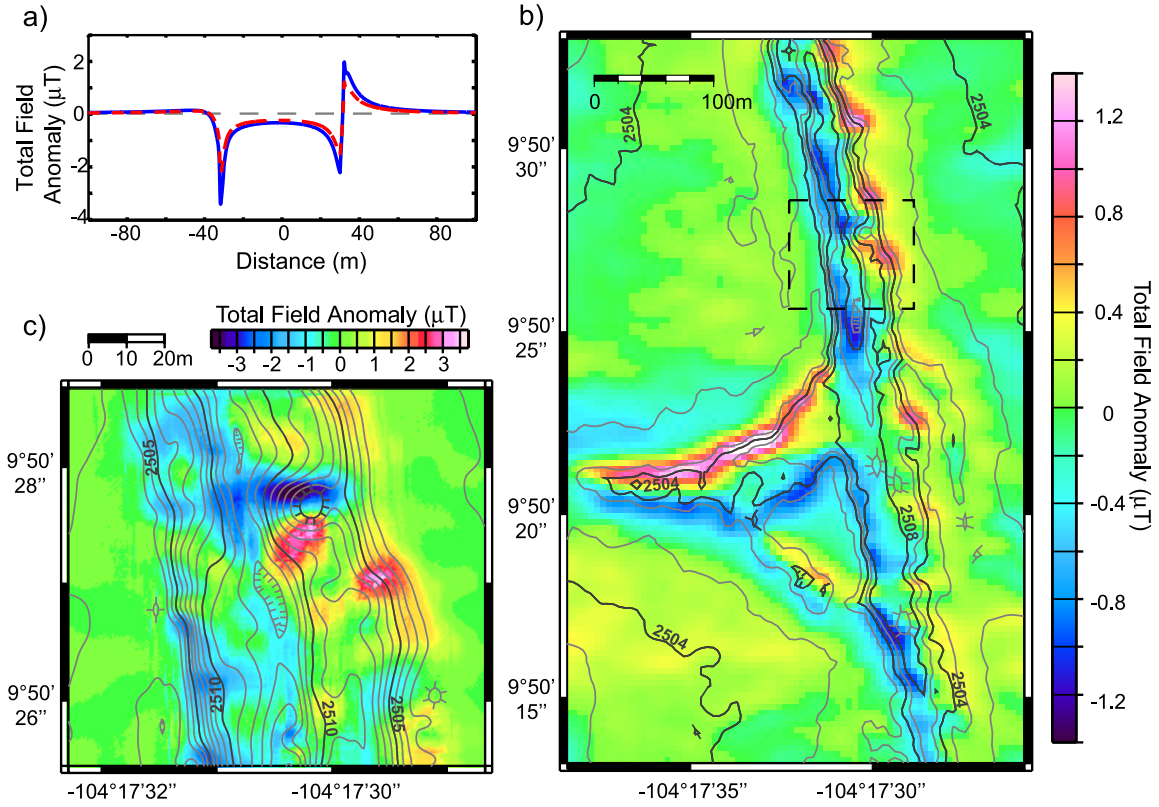

Figure 10. (a) Anomaly generated by a 2-D trough structure striking N8°W. Trough is 60 m wide and 7.5 m deep, and the walls make a 70° angle with the horizontal. Anomaly is calculated at 2 m above the bathymetry. Ambient field is the present field at 9°50′N (D = 8°, I = 32°). The 250 m thick source layer is uniformly magnetized at 20 Am^{-1} in either the expected dipole direction (dashed red line; D = 0°, I = 18.5°) or in the 1900 direction (solid blue line; D = 7°, I = 27.5°). (b) Anomaly generated by actual bathymetry near 9°50′N and calculated at 10 m above bathymetry; other parameters same as for 2-D case (magnetization in expected dipole direction). ABE microbathymetry [*Fornari et al.*, 2004] has 5 m horizontal resolution. Total field anomaly scale (μT) is shown to right, saturated at ±1.3 μT; largest anomalies are −1.17 and +1.88 μT. The 2 m contours are shown by gray lines; every other contour is bold; tick marks point in downhill direction. (c) Anomaly calculated at 2 m above bathymetry for boxed area shown in Figure 10b. Bathymetry is gridded at ∼0.5 m for modeling purposes. The 1 m contours are shown; every fifth contour is bold. Color scale is saturated at ±3.75 μT; largest anomalies are −4.14 and +3.79 μT. The 2–D and 3–D forward modeling techniques are adapted from *Blakely* [1996].

ing thermal gradient. The same process will occur during laboratory cooling, but the differential will not be as great, because the overall slope of the cooling rate versus temperature profile is related to the original thermal gradient. The net effect could lead to a small bias, but the maximum conceivable difference is a factor of 10 in cooling rate which translates into a 3–7% difference in paleointensity, or a maximum of ∼2.5 μT, certainly not enough to explain some of the more extreme values. Another result that could follow from the elevated unblocking temperatures is an increased possibility of sample alteration during the paleointensity experiments. As stated above, precipitation or growth of magnetite during the experiment could result in an underestimate of paleointensity. However, the strict requirement that we placed on the pTRM checks seems to preclude this possibility.

[41] A final possibility is that at least some of the SBG is not recording or preserving a primary thermoremanence. One of the samples with a very low paleointensity (AL2740-6, 28.7 μT) was taken from the bottom of a pillar near active vents. Other glass specimens come from samples that show evidence of interaction with a hot vapor phase [*Perfit et al.*, 2003]. It is possible that samples within the AST where flows may repeatedly intrude and drain [e.g., *Fornari et al.*, 1998, 2004], and where there is localized hydrothermal venting, may have had complicated thermal histories, leading to in situ alteration and the production of a chemical remanence (CRM). It has been suggested

that some unspecified low-temperature alteration may lead to the production of a CRM and an attendant negative bias in paleointensity results [*Heller et al.*, 2002]. However, there is nothing in the available rock magnetic or paleointensity data to distinguish these samples from others with paleointensities closer to the expected field value. It is difficult to envision an alteration mechanism that would serve to lower the paleointensity while simultaneously producing linear NRM-pTRM plots and positive pTRM checks. Any process that results in growth of magnetite on the seafloor should also result in magnetite growth in laboratory experiments, leading to failed pTRM checks. While alteration at this time does not satisfactorily explain the low paleofield values, the possibility bears further investigation.

[42] There is no reason that all of these factors may not contribute to the lower than expected paleointensity values. Some local field effects may combine with an additional contribution from a cooling rate difference, and though the exact effect of in situ alteration and a possible CRM remains unknown, it is possible certain samples are affected in ways we do not yet understand. It also seems possible that these problems are exacerbated with these specific samples either because of their magnetic properties (high unblocking temperatures) or their location within or adjacent to the AST. While few data exist for comparison, paleointensities from other locations with very recent flows (9°17′N, 9°37′N) do not seem to show a negative bias to quite the same degree, although a few samples are still "too low" at the 95% confidence level.

[43] Results from the 1991–1992 flow show that the use of paleointensity as an absolute dating tool has limitations. The uncertainty represented by the standard error of the mean clearly does not fully represent the total uncertainty in the ambient field at the time of eruption. However, by at least selecting samples from areas away from topographic extremes (as possible), avoiding areas with obviously complicated thermal histories, and by analyzing multiple samples from different parts of a flow the technique should still provide useful age information, if not at decadal-scale resolution.

5.2.2. Other Age Information

[44] Despite the uncertainties described above, there is still a significant amount of useful information to be gained from the axial samples shown in Figure 9. If we accept that there is some negative bias introduced into the data, from whatever source, then the all of the samples within 500 m of the AST between 9°46′ and 9°50.5′N are entirely consistent with eruption during the 1991–1992 event, or within a few decades of that. By contrast, just north of the 1991–1992 flow, there is a significant offset in paleointensity to higher values, as would be expected from older flows. While the AST becomes discontinuous north of ~9°51.5′N, there is nothing to suggest a consistently positive bias resulting from a terrain effect. Moreover, between ~9°50.5 and 9°55′N, the majority of the paleointensities (though more sparsely distributed spatially than to the south) are confined to a relatively narrow band of paleointensity (~40–44 μT). By comparison to the *Jackson et al.* [2000] model (and recognizing that there may be some negative bias to these site means), these values represent eruption dates of ~1875 or earlier. There are some notable exceptions to this "trend." At ~9°52′N there is a cluster of samples with very consistent values of ~37.5 μT, which, taken at face value, is consistent with an eruption date of ~1950. At ~9°53.3′N, sample 2359-4 has a paleointensity consistent with very recent (indistinguishable from present-day) eruption. This sample is described as fresher in appearance than its surroundings, and is located within ~20 m of another sample (AL2497-1B) that was dated by ^{210}Po-^{210}Pb to early 1992 [*Rubin et al.*, 1994]. It also has an elevated Mg content consistent with other samples believed to have erupted near this location during the 1992 event [*Gregg et al.*, 1996].

[45] The picture that emerges between 9°45 and 9°55′N is that that the last major eruptive period (along the axial summit) was at least ~150 years ago, followed by at least one and possibly several smaller eruptions about 50 years ago, and then by the 1991–1992 eruptions. Although the error on our paleointensity estimates is apparently larger than the formal standard error, it seems we might tentatively conclude that the recurrence interval for eruptions the size of the 1991–1992 flows or bigger is on the order of hundreds of years. We define recurrence interval here to be the average elapsed time between eruptions at a given point along the axis. It is worth noting that the boundary between these younger and older areas (~9°50.5′N in our paleointensity data) also roughly correlates to a change in flow morphology (pillows to the north, lobate and sheet flows to the south) and is close to a fourth-order ridge axis discontinuity as defined by *Haymon et al.* [1991] and *Haymon and White* [2004].

[46] The paleointensity data are also useful in highlighting clear age differences that were not otherwise obvious. For example, the two samples shown in Figure 9b between ~9°50.5 and 9°51′N (AL2770-7, AL3163-1) have paleointensities very distinct from and significantly higher than samples immediately to the south, suggesting that they were erupted as part of the earlier phase of activity. However, their elevated Mg content caused them to initially be classified with the 1991–1992 flow [*Gregg et al.*, 1996; *Rubin et al.*, 2001], and there is little in the way of observational evidence to distinguish them as older. Even given the scatter in paleointensity within the 1991–1992 flow, it is hard to reconcile these significantly higher values with eruption in the early 1990s, especially given that any significant bias seems more likely to be negative. A more detailed geochemical analysis has since distinguished these two samples from the 1991–1992 flow, but this highlights a potential pitfall in classifying flows based solely on geochemistry.

[47] As an additional interesting example, samples 2371-4 and 2371-5 from the small OSC at 9°37′N (Figures 7 and 9), have paleointensities consistent with a very recent eruption. These samples are located near the tip of the hypothesized southward propagating eastern AST [*Smith et al.*, 2001] and near low-temperature vent sites possibly associated with a 1991 eruption. However, it is not possible to unambiguously preclude that they are older with a source in the western AST limb. Their paleointensities, however, are more consistent with a source in the younger, eastern limb, if not as part of the 1991 eruption, then they are not much older. By contrast, a sample just east of the southernmost tip of the eastern AST is presumed to be older as it has a significantly higher paleointensity (~45 μT), consistent with an older appearance and enhanced Mn coating on its surface.

5.3. Across-Axis Observations

[48] To a first-order approximation (as mentioned above), the cross-axis paleointensity data (Figures 7 and 11) are consistent with the trends in paleofield variation shown in Figure 8b: near-present-day values along the AST, flanked by values higher than present-day out to ~2 km, then falling to values significantly lower than present-day at 2–4 km. These data are also largely consistent with observations, radiometric dating, and modeling suggesting flows may reach up to 2 or more kilometers from the AST, either erupting off axis, or flowing down the axial high [*Perfit et al.*, 1994; *Goldstein et al.*, 1994; *Hooft et al.*, 1996; *Schouten et al.*, 1999; *Sims et al.*, 2003, *Fornari et al.*, 2004; *Soule et al.*, 2005].

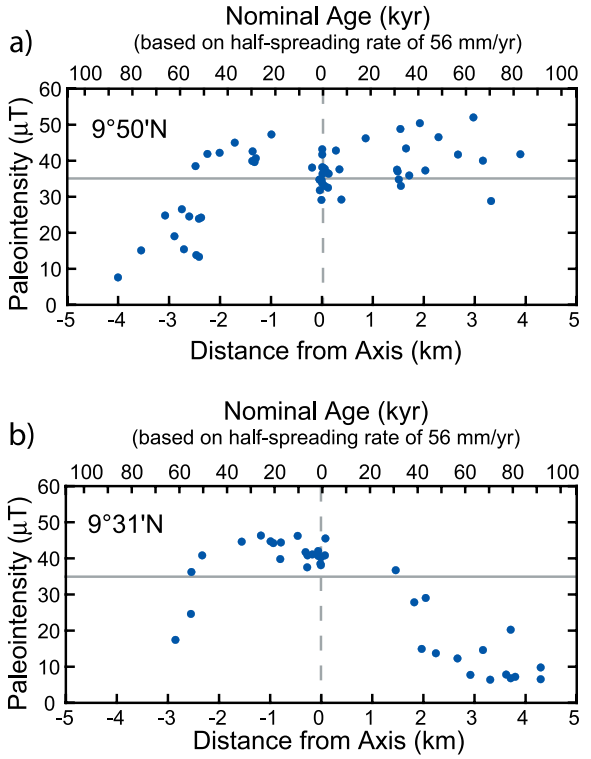

Figure 11. Paleointensity versus distance from axis for samples falling inside the sample regions at 9°31′N and 9°50′N (see Figure 7). Data are shown only for samples for which $1\sigma < 3$ μT and $N > 1$.

[49] Asymmetries in this pattern of off-axis volcanism, however, can be clearly seen in Figure 11, which plots paleointensity versus distance from the AST for samples in the 9°50′N and 9°31′N regions. At 9°50′N, a slight asymmetry can be seen in the distribution of higher than present-day paleointensity values, which according to our model represent flows erupting in the past ~500–2000 years. The high values are found up to 3–4 km on the east side of the AST (with no decrease to lower values), compared to only 2–3 km on the west side, suggesting that young flows are being deposited at locations farther from the AST on the east. Similarly, and more dramatically, the data from 9°31′N suggest that young flows have preferentially been erupted or channeled to the west of the AST. Both of these observations are consistent with analysis by *Soule et al.* [2005] that finds both an elevated number of lava channels and an asymmetry

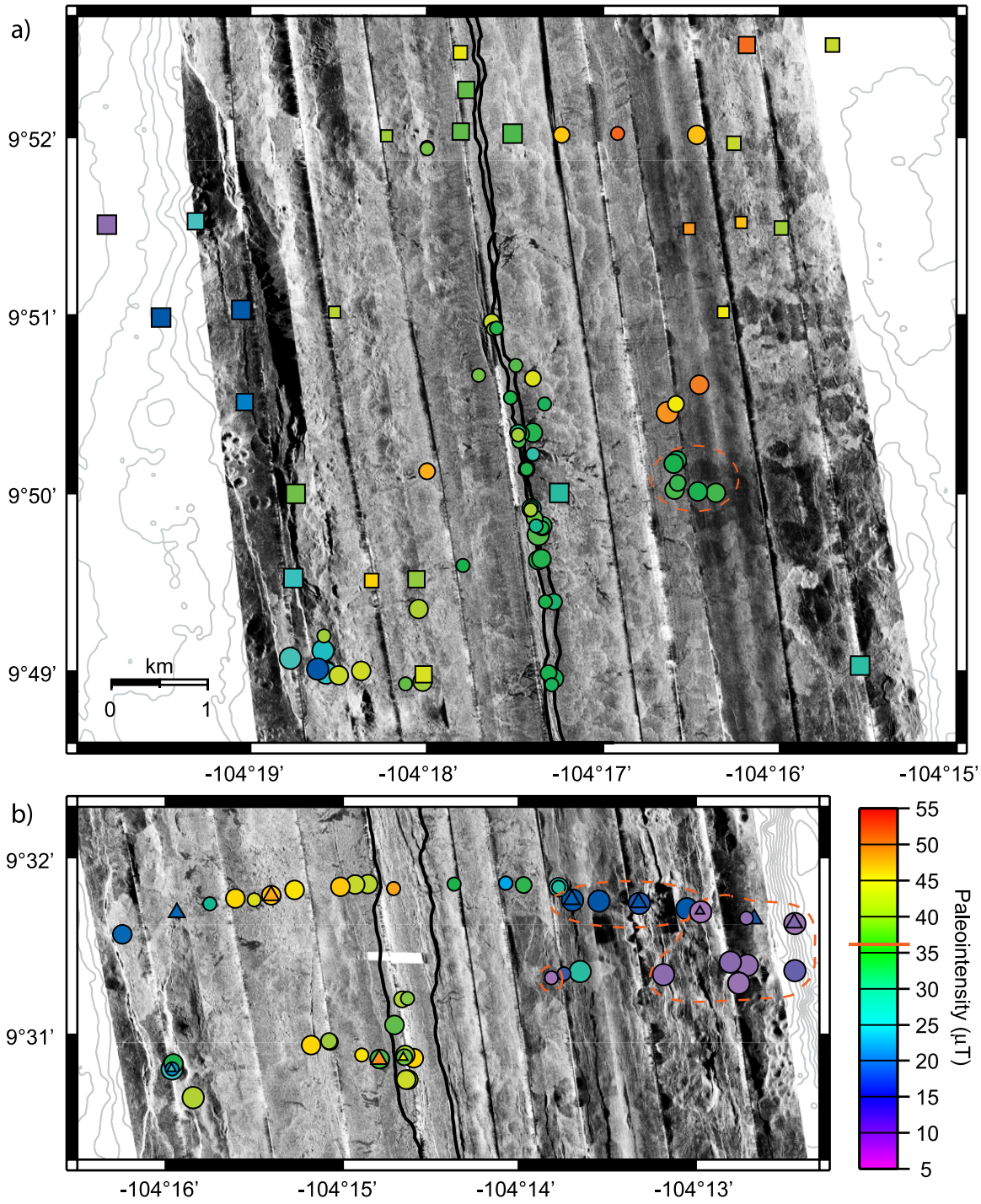

Figure 12. Enlargements of paleointensity results from (a) 9°50′N area and (b) 9°31′N area overlain on side scan data [*Schouten et al.*, 2003; *Fornari et al.*, 2004; *Soule et al.*, 2005]. Symbols are as in Figure 7, with the addition of paleointensity data from *Mejia et al.* [1996] shown in triangles: large triangles for samples with >1 paleointensity estimate; small triangles show results for single specimens only if $f > 0.7$ and $q > 50$. The 20 m contours from *Cochran et al.* [1999] are shown in light gray. Samples enclosed in red dashed lines are discussed in text.

in ridge volume biased to the east at 9°50′N and to the west at 9°30′N.

[50] Figure 12 shows enlarged views of paleointensity data in the regions around 9°50′N and 9°31′N, plotted on top of the high-resolution (DSL120) side scan sonar [*Schouten et al.*, 2003; *Fornari et al.*, 2004; *Soule et al.*, 2005]. Paleointensity data from *Mejia et al.* [1996] are also

shown in triangles, and in cases where the same samples were included in the present study, results agree within error. High-reflectivity (light) areas in the side scan are generally interpreted as younger terrain, while low-reflectivity (dark) areas correspond to older, more sedimented terrain, which is also typically characterized by more abundant faulting. The main exceptions to these generalizations are the dendritic, low-reflectivity areas emanating from the AST which correspond to lava channels floored by smooth sheet flows; though these sheet flows are usually young and glassy in appearance, they are also poor acoustic reflectors.

5.3.1. Region at 9°50′N

[51] A significant proportion of the ridge crest at 9°50′N is covered by high-reflectivity, "young" lavas out to > 3.5 km in some places (Figure 12a). Present-day to higher than present-day paleointensity values support an interpretation [*Fornari et al.*, 2004] that these flows are <2 ka. A cluster of six near-present-day values (~36 μT) is found ~0.5–1.0 km east of this boundary, hinting that these may be very recent. However, this far from the AST the paleointensity data alone cannot unambiguously restrict these flows to the past few decades. The side scan data, as well as observational evidence (M. Tivey, personal communication, 2004), tends to support a somewhat older age. Although such observational evidence can be unreliable, if true the paleointensity would suggest an age >~1000 years. This same set of samples was also taken near what is believed to be a growth fault that is restricting the eastward flow of lava, contributing to a strong, linear anomaly in the near-bottom magnetic data [*Schouten et al.*, 2002]. Samples taken from the east (AL3784-3) and west (AL3784-2) side of this fault have nearly identical paleointensities (37.6 ± 1.2 μT and 37.1 ± 2.4 μT, 1σ), which could be interpreted as representing very similar ages. However, the 1–2 m relief on the fault at this location seems to preclude this possibility.

[52] West of the AST, significantly lower than present-day values are largely consistent with low-reflectivity, older terrain. However, a group of relatively low-paleointensity samples (~15–25 μT) around 9°49′ on high-reflectivity terrain suggests that the interpretation of the high-reflectivity terrain as <2 ka may not hold strictly true. On the basis of our current understanding of field variations, these paleointensities are most likely to be >5–10 ka. Indeed, notes from these dives indicate that the samples were taken along a fault against which younger flows had ponded. The samples were taken from the old side of the fault, and observations suggest that they are greater than a few thousand years old.

5.3.2. Region at 9°31′N

[53] The 9°31′N region (Figure 12b) presents an entirely different picture. While much of the terrain west of the AST appears young on the basis of the side scan data, the east side has much lower reflectivity and appears significantly more fractured. This interpretation of the side scan data was confirmed by dive observations in 2004. The paleointensity data are consistent with these observations; the lowest paleointensities in the data set fall on the most faulted and sedimented terrain, and clear boundaries between high- and low-reflectivity are reflected in a contrast between high- and low-paleointensity values. Again, an exception is east of the AST at ~9°31.5′N where samples with relatively low (~15 μT) paleointensity values are found on ostensibly "young" (high-reflectivity) flows. Such low-paleointensity values seem unlikely to have occurred in the last 15–20 kyr, reinforcing that care must be taken interpreting age based on side scan.

5.3.3. Interpretations of Off-Axis Paleointensity

[54] Now that we have established that our paleomagnetic estimates for the off-axis samples are consistent with the geology (as interpreted by the side scan) with few exceptions, we can look at patterns within these data, focusing on the 9°31′N data. We interpret the majority of the lowest paleointensities in the data set (~6–8 μT, designated with purple in Figure 7 and circled in Figure 12b) as representative of the Laschamp excursion at ~40 ka. If this interpretation is correct, it appears that this portion of the axis was quite volcanically active at ~40 ka, emplacing flows at least ~0.7 to 2 km from the axis. Additionally, because they remain exposed, it implies that at least ~20 kyr passed before flows in this area reached as far as 2 km off axis again (based on a spreading rate of 55 mm yr^{-1}). Similarly, a series of 4 sites (aligned east-west; circled on Figure 11b) have paleointensities of 12.4–15.0 μT, and the three easternmost ones also have identical (major element) geochemistry. The combined near-identical paleointensity and geochemistry strongly suggests that these samples were erupted over a relatively short time interval (<100 years?), and may even represent the same flow. These three sites span ~1 km, again

suggesting that regardless of the time of eruption, this emplacement distance was not matched for ~18 kyr.

[55] The very low paleointensity value (6.5 μT, AL2495-3) at ~1.75 km from the AST (Figure 12b) deserves special attention. Table 1 shows that this field value is based on a single specimen, which would ordinarily lead us to question its reliability. However, a second specimen (7.8 μT, q = 26.5) was rejected because it just barely failed the pTRM test at 5.6%. Combined, these two specimens yield a site mean of 7.1 ± 0.5 μT. Given the excellent agreement between these two specimens, we are inclined to regard the result as reliable. This sample therefore cannot be associated with the Laschamp, because the nominal crustal age is ~32 ka. This nominal spreading rate age assumes constant, and symmetrical, spreading and that the current location of the AST as the center of volcanic activity has remained constant. *Fornari et al.* [2004, and manuscript in preparation] suggest this is the case given the bilateral symmetry of small to large flow fronts on either side of the AST between 9°30′ and 9°55′N. As discussed above, current data on field variations cannot preclude other low-intensity periods between 20 and 40 ka, but it seems very unlikely that values as low as 7 μT could be reached for times <20 ka. Taking 20 ka as a younger age limit for this sample would suggest an emplacement distance ≤ 0.62 km. Therefore, at least since 20 ka, there have been no flows reaching >1.74 km at this location, and on average through time the emplacement distances must have been much less.

[56] It should be noted that all of these low-paleointensity values (<15 μT) are from pillow lava samples, rather than sheet or lobate flows. This at least in part reflects a sampling bias in older terrain toward pillows which have more relief are less heavily sedimented than other flow types. Some of the pillows may represent flow fronts that originated in or near the AST, but others come from pillow ridges that are believed to erupt off-axis [*Perfit et al.*, 1994; *Perfit and Chadwick*, 1998], and may be younger than the surrounding flows. Some of the samples are normal MORB, while others have enriched MORB type chemistry that is not presently seen on-axis along this part of the EPR [*Perfit et al.*, 1994]. These samples therefore may represent a mixture of flows sourced on and off axis and may remain exposed in part because of their topography.

[57] What these patterns suggest is that, most of the time, relatively small-volume eruptions (similar, perhaps, to the 1991 flow) dominate, emplacing lava near the axis (<1 km). Occasionally (on a timescale of 10–20 kyr), enhanced volcanic activity results in material being emplaced farther (1–4 km) off axis in either a single large episode or in many smaller episodes spaced closely together in time. This is not inconsistent with geologic observations, but the timescales involved in the episodicity or periodicity may be significantly greater than suggested by other authors. In a study of the southern EPR, *Cormier et al.* [2003] suggest a waxing and waning of volcanism on timescales of several thousand years, while *Fornari et al.* [1998] propose a life cycle of AST formation (related to cycles in volcanic activity) with a timescale of thousands to ~10 kyr. These new paleomagnetic data suggests that the timescale between these periods of enhanced volcanic activity may be even greater, at least at 9°31′N.

[58] This interpretation is bolstered by limited radiometric data at both 9°50′N and 9°31′N. At 9°31′N, *Goldstein et al.* [1994] use ^{238}U-^{230}Th and ^{235}U-^{231}Pa to calculate model ages for a series of cross-axis samples at 9°31′N. They find that several samples out to 2–4 km from the axis have ages ranging from 0 to ~10 ka, up to 70 kyr younger than the spreading rate ages. However, most samples, especially east of the AST, have model ages that cluster around the spreading rate age, corresponding to eruption locations of 0–1 km from the axis. Two samples, presently located ~2 km from the AST, actually have ^{231}Pa ages older than their spreading rate age. Similarly at 9°50′N, although *Sims et al.* [2003] find radiometric ages generally indistinguishable from zero out to ~3 km from the AST, three samples have U-Th model ages almost exactly equivalent to their spreading rate ages (with large error bars, however). Both of these studies suggest at the extreme that 35 kyr or more may pass without any off-axis accretion locally. These data indicate that the width of the neovolcanic zone (as defined by recent eruptions) must vary significantly in time and space, locally remaining quite narrow (<1 km half width) for extended periods of time.

5.3.4. A Model of Lava Emplacement

[59] Both the paleointensity and the radiometric data from the 9°–10°N area suggest that the ages of the surface flows in some cases may not differ significantly from the nominal spreading age. In other cases, young flows may be emplaced up to

2–3 km from the axis, covering older flows. The surface pattern of flow ages (inferred from the paleointensity or radiometric ages) contains valuable information regarding the eruptive frequency and spatial scales of lava accretion. The latter parameter can be modeled with a stochastic lava emplacement model [e.g., *Hooft et al.*, 1996], and such models have been used to examine the pattern of lava accumulation and its relationship to seismic layer 2A. However, temporal variability in lava distribution has not yet been accommodated in such models.

[60] Although poorly constrained, eruptions on the EPR are thought to recur on the order of years to tens of years [*Haymon et al.*, 1993; *Gregg et al.*, 1996; *Perfit and Chadwick*, 1998; *Sinton et al.*, 2002]. Under the assumption of a constant spreading rate and extrusive layer thickness, an approximate eruptive recurrence interval can be calculated on the basis of flow volumes estimated from a few mapped flows along with measured eruptive fissure length. For example, detailed mapping on the southern EPR suggests an average recurrence interval of 3–14 years for a 50 km ridge segment, with associated eruptive fissures ranging from 1–18 km in length [*Sinton et al.*, 2002]. At any given point along the segment therefore the average recurrence interval would be ~15–70 years based on an eruptive fissure 10 km long. Mapped flow volumes, however, vary, and this must at some level be tied to variations in time between flows, assuming a constant extrusive layer thickness. Limited observations over a wide range of spreading rates suggests that large flows at slow to intermediate spreading ridges occur much less frequently than the smaller flows associated with fast spreading ridges [*Perfit and Chadwick*, 1998].

[61] In order to examine the role played by variation in the time between flows, we constructed a stochastic model linking variations in the volume of erupted lavas with time. The temporal spacing of flows in earlier stochastic models is directly tied to the spreading increment, and thus flows are uniformly distributed in time. A more realistic description of the temporal distribution of flows might be a Poisson process [e.g., *Klein*, 1982; *Solow*, 2001], with the wait time between flows independent of the timing of all prior flows. The extrusive layer in our model is constructed from a single distribution of lava flows, with the time between eruptions represented by a standard gamma distribution with a mean of 2 (resulting from a shape parameter of 2 and a scale parameter of 1). The median of this distribution is then scaled to the desired median time between flows, f_m, on the order of the proposed recurrence interval suggested above (15–70 years). The model allows for noneruptive spreading between flows by the simple emplacement of a dike (to the surface). The dike location (and flow center) relative to the axis is determined as a random Gaussian process with a standard deviation, σ_d.

[62] If melt is being supplied to a magma chamber at a constant rate, then withdrawal of a large volume of melt will lead to a period of decreased magmatic activity while the available volume in the magma chamber rebuilds [*Carbotte et al.*, 2003]. We therefore require that the volume of the flow be linearly related to the time since the last eruption, although in reality it is not necessary that a large volume of available melt be used in a single eruption. Flow thickness scales with the size of the flow such that the aspect ratio is equal to the number of spreading events (or time steps) prior to the flow raised to the 1.5 power. This is intended to roughly match observations linking low effusion rates with pillow mound morphology (high aspect ratio) and high effusion rates with relatively thin sheet flows [e.g., *Griffiths and Fink*, 1992; *Kurras et al.*, 2000]. Observations at the EPR also show that small volume eruptions tend to produce pillows, while larger volume eruptions may be more likely to produce lobate or sheet flows [*Perfit and Chadwick*, 1998; *Kurras et al.*, 2000]. We note that our model has no topography, so any flow regardless of thickness will be covered by the next flow reaching that location. Distributions of the time between flows, flow thickness and flow width are shown in Figures 13a–13c for an example based on 5000 realizations of this model with f_m = 70 years and σ_d = 100 m. For these calculations we use a horizontal grid spacing of 0.5 m (equivalent to time steps of ~4.5 years) and a vertical grid spacing of 1 m.

[63] As can be seen from the results of such a model (Figure 13e), small, frequent eruptions make up the bulk of the extrusive layer volumetrically, but it is the larger, less frequent eruptions that are preserved at the surface. This can result in large age contrasts in an across-axis direction, such as we see in the paleointensity data at 9°30′N, with large areas of a similar age remaining exposed at the surface. Age offsets of 10 kyr to >20 kyr are not unusual for a model with f_m = 70 years (Figure 14b). For comparison, we also show results from models with f_m = 50 years (Figure 14a) and

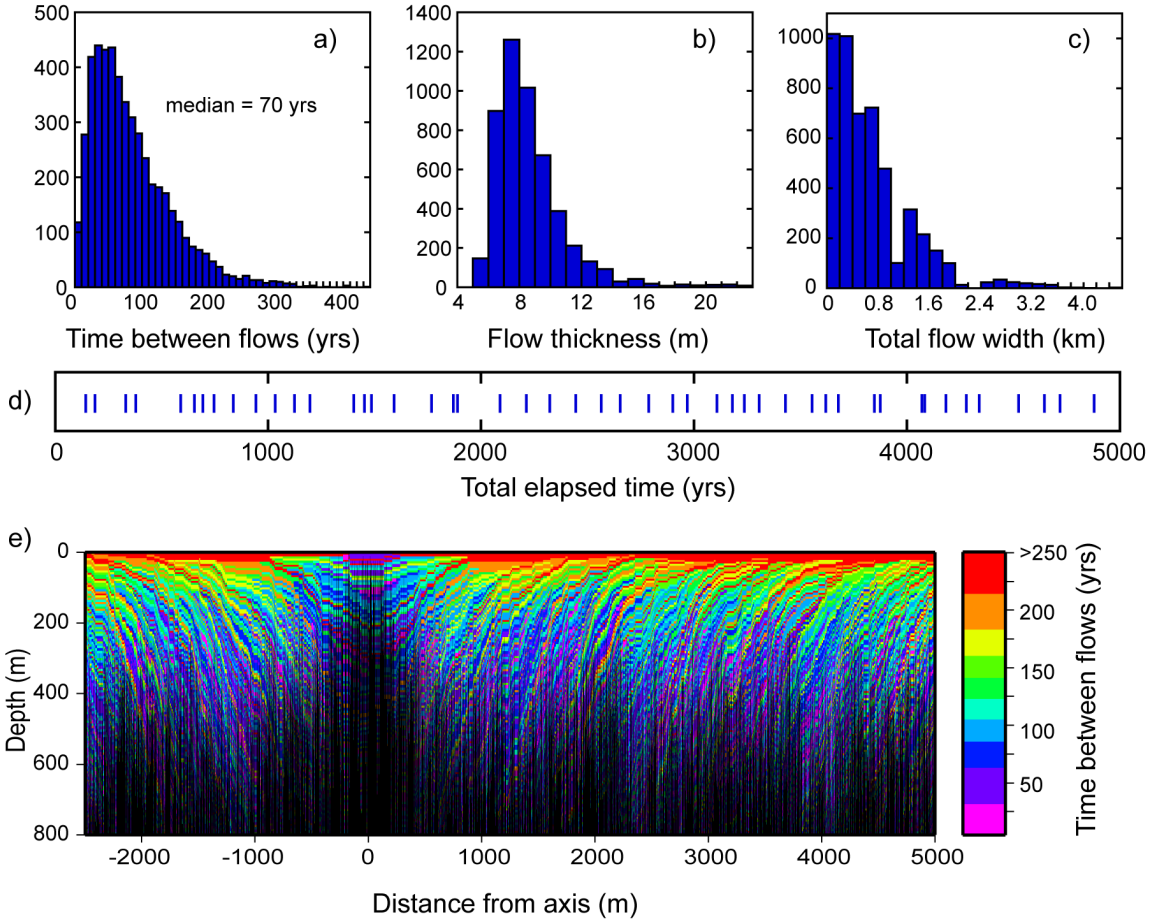

Figure 13. Stochastic unimodal lava emplacement model. Data are from 5000 realizations of the model. (a) time between successive flows taken from a standard gamma distribution (see text) with the median of the distribution scaled to the median time between flows, f_m (in this case 70 years). The flow volume is directly proportional to the time between flows. (b) Flow thickness scales with the flow volume calculated as the number of time steps since the last flow raised to the 1.5 power. (c) Total flow width. The gaps in the distribution result from forcing the flow dimensions to fit the grid spacing in the model. (d) A small subset of data demonstrating flow spacing in the time domain. Each blue bar represents an eruptive event. (e) Model results for f_m = 70 years and σ_d = 100 m. Flow color represents the amount of time elapsed since the previous flow (and is also related to flow volume). Black represents dikes.

f_m = 90 years (Figure 14c). As would be expected, the longer the median time between flows, the larger the potential age offset between adjacent flows at the surface. Similarly, the maximum distance a flow reaches from the axis increases with an increase in f_m (Figures 14d–14f). For f_m = 70 years, some flows will reach 2.0–2.5 km from the axis (a combined result of flow width and dike intrusion location). The difference between the surface flow age and the spreading rate age ranges between ~15 and 30 kyr for most of the crust away from the accretion zone (f_m = 70 years; Figure 14h). This closely matches the age differentials inferred from the paleointensity.

[64] Assuming the underlying distributions of our model approximate reality, then the situation of $f_m \approx 70$ most closely matches the range of emplacement distances and age offsets (both among surface flows and between surface flow ages and spreading rate ages) inferred from the data. With this flow distribution, flows >3.5 km total width will have an average recurrence interval of ~ 20 kyr, similar to what we estimated from the paleointensity data.

[65] While we have not attempted to match seismic layer 2A thickening with this model, we note that thickening occurs over a region ~1–2.5 km full width and the extrusive dike transition zone (defined as the vertical distance over which the crust goes from 20% to 70% dikes) ranges from ~300 m

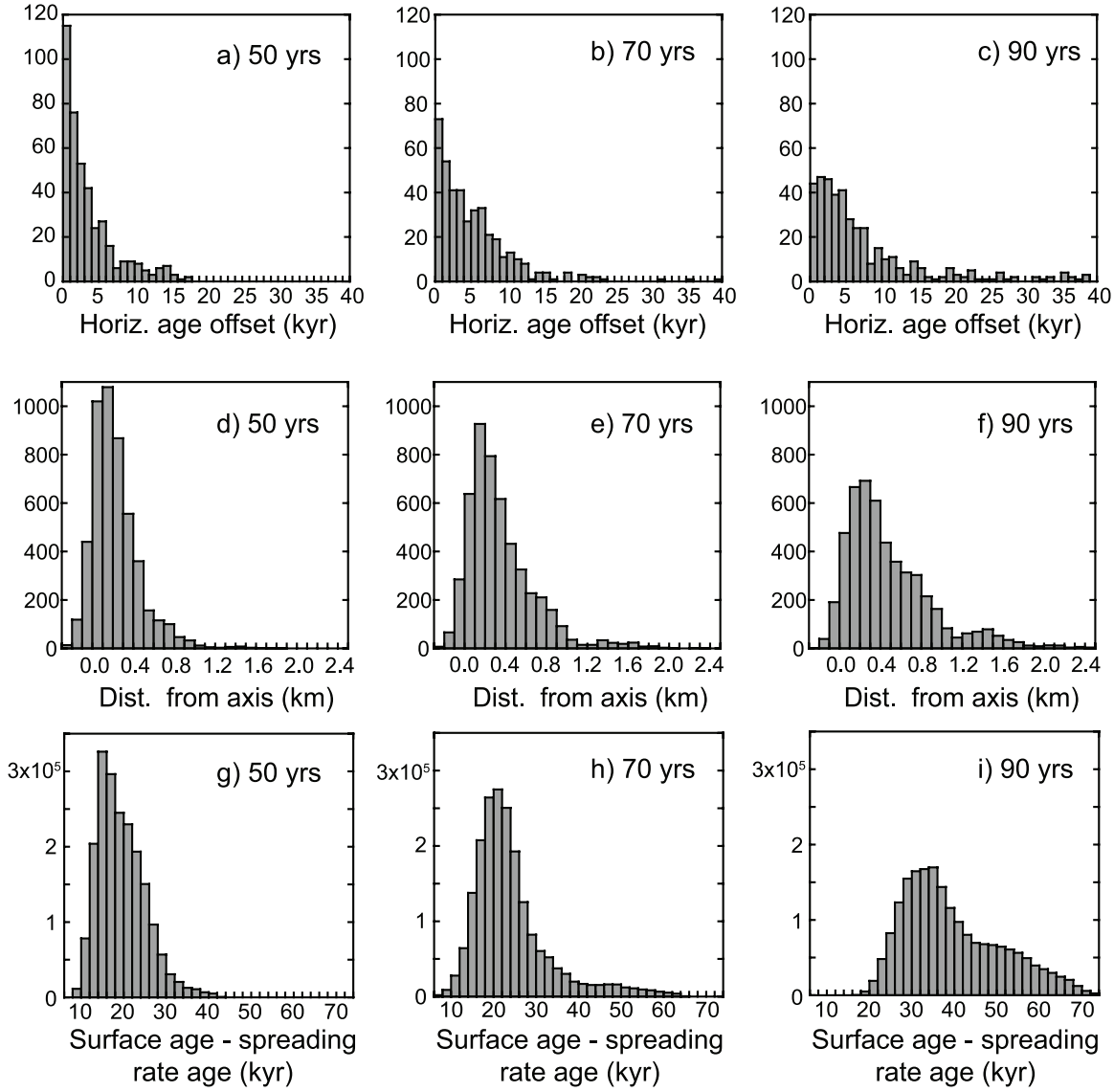

Figure 14. (a)–(c) Distribution of nonzero horizontal age offsets of surface flows for different median flow intervals (30, 50, 70 years) after letting models run long enough to get >400 age offsets. Note that the *x* axis has been truncated at 40 kyr for the 70 and 90 year models, but age offsets of up to 50 kyr are found in the 70 year model and up to 58 kyr in the 90 year model. (d)–(f) Distance of the eastern edge of each flow from the axis (at the time of emplacement). This distance takes into account both the flow width and the location of the dike injection. Negative values result from flows that were emplaced entirely on the west side of the axis. (g)–(i) Surface flow age versus crustal age based on spreading rate.

(f_m = 50 m) to ~170 m (f_m = 90 m). While these values are within the range of observations for fast spreading crust, the 2A thickening typically occurs over a somewhat wider zone, and the extrusive dike transition in ophiolites is typically somewhat less diffuse [see *Hooft et al.*, 1996, and references therein]. The zone of 2A thickening could be widened by incorporating a bimodal lava deposition scheme as by *Hooft et al.* [1996], with large flows accumulating only off axis and small flows accumulating only on axis. However, as we are primarily interested in the larger flows that remain exposed at the surface, we prefer the simplicity of the unimodal model that adequately describes our surface paleointensity data while keeping the number of free parameters small.

6. Conclusions

[66] This study provides one of the first extensive tests of paleointensity as a dating tool or temporal

marker. A large data set from a well-studied region on a fast spreading ridge has allowed us to test the resolution of the method and to integrate paleomagnetic observations with other available data to draw some conclusions about the timing and episodicity of eruptive activity on the East Pacific Rise between 9° and 10°N. Our major conclusions are as follows:

[67] 1. Results from the recent (1991–1992) volcanic eruptions at 9°50′N suggest that paleointensity estimates in SBG may be biased slightly low. The most likely explanations for this are a local field effect and a small contribution from cooling rate bias in samples with elevated unblocking temperatures. While some in situ alteration of samples with complicated thermal histories within or near the AST may have an as yet unknown effect on paleointensity, the close agreement with known field values in most cases seems to rule out CRM as the principal source of remanence.

[68] 2. Direct absolute dating using paleointensity may have limited resolution with the presently available field models; however, with a careful sampling strategy, the paleointensity method remains a very useful tool in determining approximate age differences in young flows, in addition to determining contemporaneity of flows.

[69] 3. Along axis data suggest that north of ~9°46′N, the near-axis region may be subdivided into two: a) South of ~9°50.5′N paleointensity data are consistent with flows erupted in 1991–1992, or within 1–2 decades of that time; and b) North of ~9°50.5′N, the majority of the paleointensity data are consistent with eruption >150 years ago. This leads to the conclusion that the recurrence interval for flows greater than or equal to the size of the 1991–1992 flows may be on the order of hundreds of years.

[70] 4. The spatial distribution of paleointensities can also provide information on the aerial extent and episodicity of off-axis lava emplacement. Across axis data suggest that the episodicity in extensive off-axis volcanism may be on the order of 10–20 kyr. This is supported by results of a unimodal stochastic model of lava emplacement that links eruptive volume to time between flows.

Acknowledgments

[71] This work was accomplished with support from NSF grants OCE-0095698 (J. S. G.), OCE-0095342 (D. V. K.), OCE-9912072 (M. R. P.), OCE-0138088 (M. R. P.), and OCE-9819261 (D. J. F.). This is LDEO contribution 6897. We would like to thank Winter Miller and Jason Steindorf at Scripps and Jamie Levine at LDEO for invaluable assistance with the many, many paleomagnetic measurements. We thank Maurice Tivey for providing glass samples from *Alvin* dives 3784 and 3963. We also thank Lisa Tauxe and Steve Cande for numerous helpful discussions and the journal reviewers (Rob Coe, Paul Johnson, and Andrei Kosterov) and editor John Tarduno for constructive comments.

References

Beer, J., R. Muscheler, G. Wagner, C. Laj, C. Kissel, P. W. Kubik, and H.-A. Synal (2002), Cosmogenic nuclides during isotope stages 2 and 3, *Quat. Sci. Rev.*, *21*, 1129–1139.

Bergmanis, E. C., J. M. Sinton, K. H. Rubin, J. J. Mahoney, J. Bowles, J. S. Gee, and M. C. Smith (2004), Magma reservoir dynamics and diverse mantle melting at the southern East Pacific Rise, 17°22′S–17°35′S, *Eos Trans. AGU*, *85*(47), Fall Meet. Suppl., Abstract V53A-0611.

Blakely, R. J. (1996), *Potential Theory in Gravity and Magnetic Applications*, 441 pp., Cambridge Univ. Press, New York.

Böhnel, H., J. Morales, C. Caballero, L. Alva, G. McIntosh, S. Gonzalez, and G. J. Sherwood (1997), Variation of rock magnetic parameters and paleointensities over a single Holocene lava flow, *J. Geomagn. Geoelectr.*, *49*, 523–542.

Bowles, J., J. Gee, J. A. Hildebrand, and L. Tauxe (2002), Archaeomagnetic intensity results from California and Ecuador: Evaluation of regional data, *Earth Planet. Sci. Lett.*, *203*, 967–981.

Bowles, J., J. S. Gee, D. V. Kent, E. Bergmanis, and J. Sinton (2005), Cooling rate effects on paleointensity estimates in submarine basaltic glass and implications for dating young flows, *Geochem. Geophys. Geosyst.*, *6*, Q07002, doi:10.1029/2004GC000900.

Cande, S. C., and D. V. Kent (1995), Revised calibration of the geomagnetic polarity timescale for the Late Cretaceous and Cenozoic, *J. Geophys. Res.*, *100*, 6093–6095.

Carbotte, S. M., and K. C. Macdonald (1992), East Pacific Rise 8°–10°30′N: Evolution of ridge segments and discontinuities from SeaMARC II and three-dimensional magnetic studies, *J. Geophys. Res.*, *97*, 6959–6982.

Carbotte, S. M., W. B. F. Ryan, W. Jin, M. Cormier, E. Bergmanis, J. Sinton, and S. White (2003), Magmatic subsidence of the East Pacific Rise (EPR) at 18°14′S revealed through fault restoration of ridge crest bathymetry, *Geochem. Geophys. Geosyst.*, *4*(1), 1008, doi:10.1029/2002GC000337.

Carlut, J., and D. V. Kent (2000), Paleointensity record in zero-age submarine basalt glasses: Testing a new dating technique for recent MORBs, *Earth Planet. Sci. Lett.*, *183*, 389–401.

Carlut, J., and D. V. Kent (2002), Grain-size-dependent paleointensity results from very recent mid-oceanic ridge basalts, *J. Geophys. Res.*, *107*(B3), 2049, doi:10.1029/2001JB000439.

Carlut, J., M.-H. Cormier, D. V. Kent, K. E. Donnelly, and C. H. Langmuir (2004), Timing of volcanism along the northern East Pacific Rise based on paleointensity experiments on basaltic glasses, *J. Geophys. Res.*, *109*, B04104, doi:10.1029/2003JB002672.

Carvallo, C., P. Camps, G. Ruffet, B. Henry, and T. Poidras (2003), Mono Lake or Laschamp geomagnetic event recorded from lava flows in Amsterdam Island (southeastern Indian Ocean), *Geophys. J. Int.*, *154*, 767–782.

Christeson, G. L., G. M. Purdy, and G. J. Fryer (1994), Seismic constraints on shallow crustal emplacement processes at the fast spreading East Pacific Rise, *J. Geophys. Res.*, *99*, 17,957–17,973.

Cochran, J. R., D. J. Fornari, B. J. Coakley, R. Herr, and M. A. Tivey (1999), Continuous near-bottom gravity measurements made with a BGM-3 gravimeter in DSV *Alvin* on the East Pacific Rise crest near 9°31′N and 9°50′N, *J. Geophys. Res.*, *104*, 10,841–10,861.

Coe, R. S. (1967), The determination of paleo-intensities of the Earth's magnetic field with emphasis on mechanisms which could cause non-ideal behavior in Thellier's method, *J. Geomagn. Geoelectr.*, *19*, 157–179.

Coe, R. S., S. Gromme, and E. A. Mankinen (1978), Geomagnetic paleointensities from radiocarbon-dated lava flows on Hawaii and the question of the Pacific nondipole low, *J. Geophys. Res.*, *83*, 1740–1756.

Cormier, M.-H., W. B. F. Ryan, A. K. Shah, J. Wen, A. M. Bradley, and D. R. Yoerger (2003), Waxing and waning volcanism along the East Pacific Rise on a millennium time scale, *Geology*, *31*, 633–636.

Dunlop, D., and Ö. Özdemir (1997), *Rock Magnetism: Fundamentals and Frontiers*, 573 pp., Cambridge Univ. Press, New York.

Fabian, K. (2003), Some additional parameters to estimate domain state from isothermal magnetization measurements, *Earth Planet. Sci. Lett.*, *213*, 337–345.

Fornari, D. J., R. M. Haymon, M. R. Perfit, T. K. P. Gregg, and M. H. Edwards (1998), Axial summit trough of the East Pacific Rise 9°–10°N: Geological characteristics and evolution of the axial zone on fast spreading mid-ocean ridges, *J. Geophys. Res.*, *103*, 9827–9855.

Fornari, D. J., et al. (2004), Submarine lava flow emplacement at the East Pacific Rise 9°50′N: Implications for uppermost ocean crust stratigraphy and hydrothermal fluid circulation, in *Mid-Ocean Ridges: Hydrothermal Interactions Between the Lithosphere and Oceans*, *Geophys. Monogr. Ser.*, vol. 148, edited by C. R. German, J. Lin, and L. M. Parson, pp. 187–217, AGU, Washington, D. C.

Frank, M., B. Schwarz, S. Baumann, P. W. Kubik, M. Suter, and A. Mangini (1997), A 200 kyr record of cosmogenic radionuclide production rate and geomagnetic field intensity from 10Be in globally stacked deep-sea sediments, *Earth Planet. Sci. Lett.*, *149*, 121–129.

Gee, J. S., S. C. Cande, J. A. Hildebrand, K. Donnelly, and R. L. Parker (2000), Geomagnetic intensity variations over the past 780 kyr obtained from near-seafloor magnetic anomalies, *Nature*, *408*, 827–832.

Goguitchaichvili, A., L. M. Alva-Valdivia, J. Rosas-Elguera, J. Urrutia-Fucugauchi, and J. Solé (2004), Absolute geomagnetic paleointensity after the Cretaceous Normal Superchron and just prior to the Cretaceous-Tertiary transition, *J. Geophys. Res.*, *109*, B01105, doi:10.1029/2003JB002477.

Goldstein, S. J., M. R. Perfit, R. Batiza, D. J. Fornari, and M. T. Murrell (1994), Off-axis volcanism at the East Pacific Rise detected by uranium-series dating of basalts, *Nature*, *367*, 157–159.

Gregg, T. K. P., D. J. Fornari, M. R. Perfit, R. M. Haymon, and J. H. Fink (1996), Rapid emplacement of a mid-ocean ridge lava flow on the East Pacific Rise at 9°46′–51′N, *Earth Planet. Sci. Lett.*, *144*, E1–E7.

Grevemeyer, I., N. Kaul, H. Villinger, and W. Weigel (1999), Hydrothermal activity and the evolution of the seismic properties of upper oceanic crust, *J. Geophys. Res.*, *104*, 5069–5079.

Griffiths, R. W., and J. H. Fink (1992), Solidification and morphology of submarine lavas: A dependence on extrusion rate, *J. Geophys. Res.*, *97*, 19,729–19,737.

Guillou, H., B. S. Singer, C. Laj, C. Kissel, S. Scaillet, and B. R. Jicha (2004), On the age of the Laschamp geomagnetic excursion, *Earth Planet. Sci. Lett.*, *227*, 331–343.

Guyodo, Y., and J.-P. Valet (1999), Global changes in intensity of the Earth's magnetic field during the past 800 kyr, *Nature*, *399*, 249–252.

Harding, A. J., G. M. Kent, and J. A. Orcutt (1993), A multichannel seismic investigation of upper crustal structure at 9°N on the East Pacific Rise: Implications for crustal accretion, *J. Geophys. Res.*, *98*, 13,925–13,944.

Haymon, R. M., and S. M. White (2004), Fine-scale segmentation of volcanic/hydrothermal systems along fast-spreading ridge crests, *Earth Planet. Sci. Lett.*, *226*, 367–382.

Haymon, R. M., D. J. Fornari, M. H. Edwards, S. Carbotte, D. Wright, and K. C. Macdonald (1991), Hydrothermal vent distribution along the East Pacific Rise crest (9°09′–54′N) and its relationship to magmatic and tectonic processes on fast-spreading mid-ocean ridges, *Earth Planet. Sci. Lett.*, *104*, 513–534.

Haymon, R. M., et al. (1993), Volcanic eruption of the mid-ocean ridge along the East Pacific Rise crest at 9°45–52′N: Direct submersible observations of the seafloor phenomena associated with an eruption event in April, 1991, *Earth Planet. Sci. Lett.*, *119*, 85–101.

Heller, R., R. T. Merrill, and P. L. McFadden (2002), The variation of intensity of Earth's magnetic field with time, *Phys. Earth Planet. Inter.*, *131*, 237–249.

Hooft, E. E. E., H. Schouten, and R. S. Detrick (1996), Constraining crustal emplacement processes from the variation in seismic layer 2A thickness at the East Pacific Rise, *Earth Planet. Sci. Lett.*, *142*, 289–309.

Jackson, A., A. R. T. Jonkers, and M. R. Walker (2000), Four centuries of geomagnetic secular variation from historical records, *Philos. Trans. R. Soc. London, Ser. A*, *358*, 957–990.

Klein, F. W. (1982), Patterns of historical eruptions at Hawaiian volcanoes, *J. Volcanol. Geotherm. Res.*, *12*, 1–35.

Korte, M., and C. G. Constable (2005), The geomagneticdipole moment over the last 7000 years—New results from a global model, *Earth Planet. Sci. Lett.*, *236*, 348–358.

Kurras, G. J., D. J. Fornari, M. H. Edwards, M. R. Perfit, and M. C. Smith (2000), Volcanic morphology of the East Pacific Rise crest 9°49′–52′: Implications for volcanic emplacement processes at fast-spreading mid-ocean ridges, *Mar. Geophys. Res.*, *21*, 23–41.

Laj, C., C. Kissel, A. Mazaud, J. E. T. Channel, and J. Beer (2000), North Atlantic palaeointensity stack since 75 ka (NAPIS-75) and the duration of the Laschamp event, *Philos. Trans. R. Soc. London, Ser. A*, *358*, 1009–1025.

Laj, C., C. Kissel, V. Scao, J. Beer, D. M. Thomas, H. Guillou, R. Muscheler, and G. Wagner (2002), Geomagnetic intensity and inclination variations at Hawaii for the past 98 kyr from core SOH-4 (Big Island): A new study and a comparison with existing contemporary data, *Phys. Earth Planet. Inter.*, *129*, 205–243.

Laj, C., C. Kissel, and J. Beer (2004), High resolution global paleointensity stack since 75 kyr (GLOPIS-75) calibrated to absolute values, in *Timescales of the Paleomagnetic Field*, *Geophys. Monogr. Ser.*, vol. 145, edited by J. E. T. Channell et al., pp. 255–265, AGU, Washington, D. C.

Lanci, L., and D. V. Kent (2003), Introduction of thermal activation in forward modeling of hysteresis loops for single-domain magnetic particles and implications for the

interpretation of the Day diagram, *J. Geophys. Res.*, *108*(B3), 2142, doi:10.1029/2001JB000944.

Levi, S., H. Audunsson, R. A. Duncan, L. Kristjansson, P.-Y. Gillot, and S. P. Jakobsson (1990), Late Pleistocene geomagnetic excursion in Icelandic lavas: Confirmation of the Laschamp excursion, *Earth Planet. Sci., Lett.*, *97*, 443–457.

Lund, S. P., M. Schwartz, L. Keigwin, and T. Johnson (2005), Deep-sea sediment records of the Laschamp geomagnetic field excursion (~40,000 calendar years before present), *J. Geophys. Res.*, *110*, B04101, doi:10.1029/2003JB002943.

Macdonald, K. C., and P. J. Fox (1988), The axial summit graben and cross-sectional shape of the East Pacific Rise as indicators of axial magma chambers and recent volcanic eruptions, *Earth Planet. Sci. Lett.*, *88*, 119–131.

Macdonald, K. C., J.-C. Sempere, and P. J. Fox (1984), East Pacific Rise from Siqueiros to Orozco fracture zones: Along-strike continuity of axial Neovolcanic zone and structure and evolution of overlapping spreading centers, *J. Geophys. Res.*, *89*, 6049–6069.

Macdonald, K. C., et al. (1992), The East Pacific Rise and its flanks 8°–18°N: History of segmentation, propagation and spreading direction based on SeaMARC II and Sea Beam studies, *Mar. Geophys. Res.*, *14*, 299–344.

Macdougall, J. D. (1995), Using short-lived U and Th series isotopes to investigate volcanic processes, *Annu. Rev. Earth Planet. Sci.*, *23*, 143–167.

Mankinen, E. A., and D. E. Champion (1993a), Broad trends in geomagnetic paleointensity on Hawaii during Holocene time, *J. Geophys. Res.*, *98*, 7959–7976.

Mankinen, E. A., and D. E. Champion (1993b), Latest Pleistocene and Holocene geomagnetic paleointensity on Hawaii, *Science*, *262*, 412–416.

McClain, J. S., J. A. Orcutt, and M. Burnett (1985), The East Pacific Rise in cross section: A seismic model, *J. Geophys. Res.*, *90*, 8627–8639.

Mejia, V., N. D. Opdyke, and M. R. Perfit (1996), Paleomagnetic field intensity recorded in submarine basaltic glass from the East Pacific Rise, the last 69 ka, *Geophys. Res. Lett.*, *23*, 475–478.

Morales, J. M., A. Goguitchaichvili, and J. Urrutia-Fucugauchi (2001), A rock-magnetic and paleointensity study of some Mexican volcanic lava flows during the latest Pleistocene to the Holocene, *Earth Planets Space*, *53*, 893–902.

Morales, J., A. Goguitchaichvili, E. Cañon-Tapia, and R. Negrete (2003), Further absolute geomagnetic paleointensities from Baja California: Evaluation of Pliocene and early/middle Pleistocene data, *C. R. Geosci.*, *335*, 995–1004.

Perfit, M. R., and W. W. Chadwick (1998), Magmatism at mid-ocean ridges: Constraints from volcanological and geochemical investigations, in *Faulting and Magmatism at Mid-Ocean Ridges*, *Geophys. Monogr. Ser.*, vol. 106, edited by W. R. Buck et al., pp. 59–115, AGU, Washington, D. C.

Perfit, M. R., D. J. Fornari, M. C. Smith, J. F. Bender, C. H. Langmuir, and R. M. Haymon (1994), Small-scale spatial and temporal variations in mid-ocean ridge crest magmatic processes, *Geology*, *22*, 375–379.

Perfit, M. R., J. R. Cann, D. J. Fornari, J. Engels, D. K. Smith, W. I. Ridley, and M. H. Edwards (2003), Interaction of sea water and lava during submarine eruptions at mid-ocean ridges, *Nature*, *246*, 62–65.

Pick, T., and L. Tauxe (1993), Geomagnetic paleointensities during the Cretaceous normal superchron measured using submarine basaltic glass, *Nature*, *366*, 238–242.

Pick, T., and L. Tauxe (1994), Characteristics of magnetite in submarine basaltic glass, *Geophys. J. Int.*, *119*, 116–128.

Pullaiah, G., E. Irving, K. L. Buchan, and D. J. Dunlop (1975), Magnetization changes caused by burial and uplift, *Earth Planet. Sci. Lett.*, *28*, 133–143.

Reimer, P. J., et al. (2004), IntCal04 terrestrial radiocarbon age calibration, 26–0 ka BP, *Radiocarbon*, *46*, 1029–1058.

Reynolds, J. R., and C. H. Langmuir (2000), Identification and implications of off-axis lava flows around the East Pacific Rise, *Geochem. Geophys. Geosyst.*, *1*(6), doi:10.1029/1999GC000033.

Roperch, P., N. Bonhommet, and S. Levi (1988), Paleointensity of the Earth's magnetic field during the Laschamp excursion and its geomagnetic implications, *Earth Planet. Sci. Lett.*, *88*, 209–219.

Rubin, K. H., and J. D. Macdougall (1990), Dating of neovolcanic MORB using (^{226}Ra/^{230}Th) disequilibrium, *Earth Planet. Sci. Lett.*, *101*, 313–322.

Rubin, K. H., J. D. Macdougall, and M. R. Perfit (1994), ^{210}Po-^{210}Pb dating of recent volcanic eruptions on the sea floor, *Nature*, *368*, 841–844.

Rubin, K. H., M. C. Smith, E. C. Bergmanis, M. R. Perfit, J. M. Sinton, and R. Batiza (2001), Geochemical heterogeneity within mid-ocean ridge lava flows: Insights into eruption, emplacement and global variations in magma generation, *Earth Planet. Sci. Lett.*, *188*, 349–367.

Rubin, K. H., I. Van der Zander, M. C. Smith, and E. C. Bergmanis (2005), Minimum speed limit for ocean ridge magmatism from ^{210}Pb-^{226}Ra-^{230}Th disequilibria, *Nature*, *437*, 534–538.

Schouten, H., M. A. Tivey, D. J. Fornari, and J. R. Cochran (1999), Central anomaly magnetization high: Constraints on the volcanic construction and architecture of seismic layer 2A at a fast-spreading mid-ocean ridge, the EPR at 9°30′–50′N, *Earth Planet. Sci. Lett.*, *169*, 37–50.

Schouten, H., M. Tivey, D. Fornari, D. Yoerger, A. Bradley, P. Johnson, M. Edwards, and T. Kurokawa (2002), Lava transport and accumulation processes on EPR 9 27′N to 10N: Interpretations based on recent near-bottom sonar imaging and seafloor observations using ABE, Alvin and a new digital deep sea camera, *Eos Trans. AGU*, *83*(47), Fall Meet. Suppl., Abstract T11C-1262.

Schouten, H., M. A. Tivey, D. J. Fornari, D. Yoerger, A. Bradley, M. Edwards, and P. Johnson (2003), Central anomaly magnetization high: Constraints on the volcanic construction and architecture of young upper oceanic crust, EPR 9°–10°N, *Ridge2000 Events*, *1*, 30–34.

Selkin, P. A., and L. Tauxe (2000), Long-term variations in palaeointensity, *Philos. Trans. R. Soc. London, Ser. A*, *358*, 1065–1088.

Sims, K. W. W., et al. (2002), Chemical and isotopic constraints on the generation and transport of magma beneath the East Pacific Rise, *Geochim. Cosmochim. Acta*, *66*, 3481–3504.

Sims, K. W. W., et al. (2003), Aberrant youth: Chemical and isotopic constraints on the origin of off-axis lavas from the East Pacific Rise, 9°–10°N, *Geochem. Geophys. Geosyst.*, *4*(10), 8621, doi:10.1029/2002GC000443.

Sinton, J., E. Bergmanis, K. Rubin, R. Batiza, T. K. P. Gregg, K. Grönvold, K. C. Macdonald, and S. M. White (2002), Volcanic eruptions on mid-ocean ridges: New evidence from the superfast spreading East Pacific Rise, 17°–19°S, *J. Geophys. Res.*, *107*(B6), 2115, doi:10.1029/2000JB000090.

Smirnov, A. V., and J. A. Tarduno (2003), Magnetic hysteresis monitoring of Cretaceous submarine basaltic glass during Thellier paleointensity experiments: Evidence for alteration and attendant low field bias, *Earth Planet. Sci. Lett.*, *206*, 571–585.

Smith, M. C., M. R. Perfit, D. J. Fornari, W. I. Ridley, M. H. Edwards, G. J. Kurras, and K. L. Von Damm (2001), Magmatic processes and segmentation at a fast spreading mid-ocean ridge: Detailed investigation of an axial discontinuity on the East Pacific Rise crest at 9°37′N, *Geochem. Geophys. Geosyst.*, *2*(10), doi:10.1029/2000GC000134.

Sohn, R. A., S. C. Webb, and J. A. Hildebrand (2004), Fine-scale seismic structure of the shallow volcanic crust on the East Pacific Rise at 9°50′N, *J. Geophys. Res.*, *109*, B12104, doi:10.1029/2004JB003152.

Solow, A. R. (2001), An empirical Bayes analysis of volcanic eruptions, *Math. Geol.*, *33*, 95–102.

Soule, S. A., D. J. Fornari, M. R. Perfit, M. A. Tivey, W. I. Ridley, and H. Schouten (2005), Channelized lava flows at the East Pacific Rise crest 9°–10°N: The importance of off-axis lava transport in developing the architecture of young oceanic crust, *Geochem. Geophys. Geosyst.*, *6*, Q08005, doi:10.1029/2005GC000912.

Stacey, F. D., and S. K. Banerjee (1974), *The Physical Principles of Rock Magnetism*, 195 pp., Elsevier, New York.

Stuiver, M., and P. J. Reimer (1993), Extended ^{14}C database and revised CALIB radiocarbon calibration program, *Radiocarbon*, *35*, 215–230.

Tauxe, L., and H. Staudigel (2004), Strength of the geomagnetic field in the Cretaceous Normal Superchron: New data from submarine basaltic glass of the Troodos Ophiolite, *Geochem. Geophys. Geosyst.*, *5*, Q02H06, doi:10.1029/2003GC000635.

Tauxe, L., T. A. T. Mullender, and T. Pick (1996), Potbellies, wasp-waists, and superparamagnetism in magnetic hysteresis, *J. Geophys. Res.*, *101*, 571–583.

Teanby, N., C. Laj, D. Gubbins, and M. Pringle (2002), A detailed palaeointensity and inclination record from drill core SOH1 on Hawaii, *Phys. Earth Planet. Inter.*, *131*, 101–140.

Thellier, E., and O. Thellier (1959), Sur l'intensité du champ magnétique terrestre dans le passé historique et géologique, *Ann. Geophys.*, *15*, 285–378.

Vera, E. E., and J. B. Diebold (1994), Seismic imaging of oceanic layer 2A between 9°30′N and 10°N on the East Pacific Rise from two-ship wide-aperture profiles, *J. Geophys. Res.*, *99*, 3031–3041.

White, S. M., R. M. Haymon, D. J. Fornari, M. R. Perfit, and K. C. Macdonald (2002), Correlation between volcanic and tectonic segmentation of fast-spreading ridges: Evidence from volcanic structures and lava flow morphology on the East Pacific Rise at 9°–10°N, *J. Geophys. Res.*, *107*(B8), 2173, doi:10.1029/2001JB000571.

Yang, S., H. Odah, and J. Shaw (2000), Variations in the geomagnetic dipole moment over the last 12000 years, *Geophys. J. Int.*, *140*, 158–162.

Yu, Y., and L. Tauxe (2005), On the use of magnetic transient hysteresis in paleomagnetism for granulometry, *Geochem. Geophys. Geosyst.*, *6*, Q01H14, doi:10.1029/2004GC000839.

Zhou, W., R. Van der Voo, D. R. Peacor, and Y. Zhang (2000), Variable Ti-content and grain size of titanomagnetite as a function of cooling rate in very young MORB, *Earth Planet. Sci. Lett.*, *179*, 9–20.